Crustal structure of the Western U.S. from Rayleigh and Love wave amplification data

William Howard Sturgeon[1], Ana M. G. Ferreira[1], Augustin Marignier[1], and Lewis Schardong[2]

[1]University College London
[2]The Geological Survey of Israel, Jerusalem, Israel

December 8, 2022

Abstract

We present SWUS-crust, a three-dimensional shear-wave velocity model of crustal structure in the western U.S. We use Rayleigh wave amplification measurements in the period range of 38-114 s, along with Love wave amplification measurements in the period range of 38-62 s, with the latter being inverted for the first time for crustal velocity structure. Amplification measurements have narrower depth sensitivity when compared to more traditional seismic observables such as surface wave dispersion measurements. In particular, we take advantage of the strong sensitivity of Love wave amplification measurements to the crust. We invert over 6,400 multi-frequency measurements using the Monte-Carlo based Neighbourhood Algorithm, which allows for uncertainty quantification. SWUS-crust confirms several features observed in previous models, such as high-velocity anomalies beneath the Columbia basin and low-velocity anomalies beneath the Basin and Range province. Certain features are sharpened in our model, such as the northern border of the High-Lava Plains in southern Oregon in the middle crust.

Crustal structure of the Western U.S. from Rayleigh and Love wave amplification data

William Sturgeon[1], Ana M.G. Ferreira[1,2], Lewis Schardong[3], Augustin Marignier[1,4]

[1]Department of Earth Sciences, Faculty of Mathematical & Physical Sciences, University College London, WC1E 6BT, UK
[2]CERIS, Instituto Superior Técnico, Universidade de Lisboa, Av. Rovisco Pais 1, 1049-001 Lisboa, Portugal
[3]The Geological Survey of Israel, Jerusalem, Israel
[4]Mullard Space Science Laboratory, University College London, RH5 6NT, UK

Key Points:

- We present SWUS-crust, a new crustal model of the western U.S.
- Love wave amplification measurements are used for the first time and are jointly inverted with Rayleigh wave amplification measurements.
- We image well-known features and sharpen others, such as beneath the High Lava Plains.

Corresponding author: William Sturgeon, `william.sturgeon.12@ucl.ac.uk`

Abstract

We present SWUS-crust, a three-dimensional shear-wave velocity model of crustal structure in the western U.S. We use Rayleigh wave amplification measurements in the period range of 38-114 s, along with Love wave amplification measurements in the period range of 38-62 s, with the latter being inverted for the first time for crustal velocity structure. Amplification measurements have narrower depth sensitivity when compared to more traditional seismic observables such as surface wave dispersion measurements. In particular, we take advantage of the strong sensitivity of Love wave amplification measurements to the crust. We invert over 6,400 multi-frequency measurements using the Monte-Carlo based Neighbourhood Algorithm, which allows for uncertainty quantification. SWUS-crust confirms several features observed in previous models, such as high-velocity anomalies beneath the Columbia basin and low-velocity anomalies beneath the Basin and Range province. Certain features are sharpened in our model, such as the northern border of the High-Lava Plains in southern Oregon in the middle crust.

Plain Language Summary

When an earthquake ruptures, seismic surface waves called Rayleigh and Love waves travel along the Earth's surface. Seismometers on the Earth's surface record ground motions caused by the passing seismic waves. The amplitude of these waves contains information about the local Earth structure beneath the station, from which we can produce images of the Earth's interior. Whilst Rayleigh waves have previously been used to image the Earth's upper mantle, this study represents the first time that Love waves have been used, resulting in a new crustal model of the western U.S., called SWUS-crust. The model correlates with many well-known surface tectonic features, such as the Columbia Basin, Basin & Range province and Colorado Plateau. We also highlight certain features that have not been seen clearly in previous models, such as the High-Lava Plains in southern Oregon.

1 Introduction

Seismic imaging plays a crucial role in probing the structure and composition of the Earth's crust, especially when combined with laboratory measurements of crustal rocks (e.g., Christensen & Mooney, 1995; Rudnick & Gao, 2014). Seismic images of the Earth's crust are also useful for seismic hazard assessment (e.g., by providing key input information for accurate ground motion simulations) and are crucial for accurate earthquake source modelling (e.g., Frietsch et al., 2021). Moreover, removing the effects of the heterogeneous crust on seismic measurements can help constrain mantle structure (e.g., Ferreira et al., 2010; Schaeffer & Lebedev, 2015).

There are several global models of the crust, including CRUST1.0 (Laske et al., 2012), LITHO1.0 (Pasyanos et al., 2014) and the more recent model of Szwillus et al. (2019). These models constrain crustal seismic velocities on a $1^\circ \times 1^\circ$ grid scale and are mainly based on compilations of existing seismic and geophysical information, as well as on the modelling of seismic data. However, higher resolution models can be achieved on a regional scale. The dense network of EarthScope's USArray, which ended in 2021 (http://www.usarray.org/), provides an opportunity to image the local crust in finer detail across the continental U.S. (e.g., Schmandt & Humphreys, 2011; Porter et al., 2016). In particular, the western U.S. is an interesting study region due to its complex geological history and its wide range of tectonic provinces.

Crustal thickening through tectonics across the western United States was largely controlled by the subduction of the Farallon plate in the late Mesozoic and Cenozoic (e.g., Schellart et al., 2010). Progressive subduction over the past >150 Ma caused major tectonic uplift and magmatism throughout the region (e.g., Humphreys & Coblentz, 2007). In the Cretaceous, subduction of the Farallon plate produced volcanism in the crust, eventually forming the Sierra Nevada batholith (Bateman & Eaton, 1967). Later, the Laramide orogeny is thought to have been responsible for crustal thickening and uplift of the Rocky Mountains range and of the Colorado Plateau in the east, which remains largely undeformed since the early Cenozoic compression and extension (e.g., Tesauro et al., 2014). Further north, subduction also formed the Cascade Mountain range through crustal thickening, which is home to a belt of Quaternary volcanoes above the Juan de Fuca plate subduction zone (Hildreth, 2007). In the Miocene, changes in the geometry of the Farallon slab led to extension and crustal thinning. The thinned crust of the North Basin & Range (Huber, 1981) produced low elevations across the area (e.g., Braile et al., 1989) and renewed volcanic activity (e.g., Stewart, 1980), but also increased elevations along the Sierra Nevada mountain range. Further north, intense magmatism about 17 Ma formed the Columbia Basin, a large igneous province caused by basaltic volcanism (e.g., Christiansen et al., 2002). Recent magmatism also marks the High Lava Plains (HLP in Figure 1) in south-eastern Oregon, the Snake River Plain (SRP in Figure 1) and the Yellowstone hotspot. Given such complex tectonic evolution, overall the western US shows a wide range of crustal structure, from thin crust in the Basin & Range ($\sim$ 25 km) and along the Pacific border ($\sim$ 20 km), to intermediate crustal thickness values in the Columbia Basin ($\sim$ 35 km) and thick crust beneath Rocky Mountains ($\sim$ 50 km) (Laske et al., 2013).

Many previous studies have utilised the large amount of available data from the USArray to image the crustal structure of the western U.S.. Surface wave ambient noise tomography has been one of the most widely used techniques to image shear-wave velocity in the crust (e.g., Shapiro et al., 2005; Bensen et al., 2009; Moschetti et al., 2007; Lin et al., 2008; Schmandt et al., 2015; Xie et al., 2018; Porter et al., 2016). In addition to ambient noise, receiver functions have also been commonly included to improve the depth-resolution of crustal layers (e.g., Shen et al., 2013; Schmandt et al., 2015; Chai et al., 2015). To further improve sensitivity to the crust, Rayleigh wave ellipticity measurements have also been included in more recent studies (e.g., Shen & Ritzwoller, 2016; Lin et al., 2014). Moreover, Pn waves (P waves trapped below the Moho) have also been used to constrain crustal and uppermost mantle structure in the U.S. For example, Buehler and Shearer (2012) used Pn measurements in the western US to estimate crustal thickness variations and velocity perturbations just below the Moho. More recently, Tesauro et al. (2014) used a variety of seismic data types, including Pn measurements, to constrain crustal depth, crustal P-wave velocity maps and Pn velocity maps beneath the U.S.

Another seismic observable that has recently received some attention is surface wave amplification, which carries information on how surface wave amplitudes change due to the local mantle and crustal structure at a given location (e.g., Eddy & Ekström, 2014). Recent studies have shown that surface wave amplification measurements have the potential for higher-resolution imaging when compared to surface wave dispersion measurements (e.g., Eddy & Ekström, 2014; Schardong et al., 2019). Surface wave amplification has been measured in a few studies. Taylor et al. (2009) measured site amplification factors using ambient noise in California using a standing-wave methodology. Later, Lin et al. (2012) measured receiver-side amplification across the USArray using fundamental mode Rayleigh waves with a method similar to Eikonal and Helmholtz tomography. Eddy and Ekström (2014) developed a novel method to measure local amplification using amplitude ratios at nearby stations, which we will discuss in more detail later in this study. Schardong et al. (2019) built upon the methodology of Eddy and Ekström (2014) to generate a new dataset of amplification measurements across the western U.S. for vertical-and horizontal-component Rayleigh waves and Love waves in the period range between T $\sim$ 38 s and T $\sim$ 114 s. This study was the first to invert amplification measurements for crustal and mantle shear-wave velocity structure in the western U.S. The resulting model, SWUS-amp, used vertical-component Rayleigh wave amplification measurements to constrain mantle shear-wave velocity down to $\sim$300 km depth. However, the crust was only parameterised using a single layer between the Moho and surface since the data used could not constrain more complex crustal models (Figure S1).

In this study we combine Love and Rayleigh wave amplification measurements to constrain crustal shear-wave velocity in the western U.S. Love waves have a particularly strong sensitivity to crustal structure, which is explored in this work. The Love wave measurements are jointly inverted with Rayleigh wave amplification measurements to build 1-D shear-wave velocity models beneath each considered station in the western USArray. Then, these 1-D profiles are interpolated to build a new 3-D shear-wave speed model of the crust, SWUS-crust. Finally, we interpret the features imaged in SWUS-crust and compare them to those reported in other recent studies.

2 Surface wave amplification measurements

2.1 Seismic data

We use fundamental-mode vertical-component Rayleigh (hereafter referred simply as Rayleigh waves) and Love wave amplitude anomalies. Both datasets were measured using the mode-branch stripping technique (van Heijst & Woodhouse, 1997). The Rayleigh wave dataset has also been used in global studies of attenuation (Bao et al., 2016; Dalton et al., 2017) and in the study of Schardong et al. (2019), which determined crustal and upper mantle shear-wave velocity beneath the western U.S. This dataset contains data from the Transportable Array, which was part of the larger USArray between 2004 to 2007. The dataset is based on 7,744 earthquakes with M $>$ 5.0 that occurred in 2004-2007, recorded at 351 stations in the western U.S. Figure 1 shows the locations of the stations used in this study and their networks. Rayleigh waves are measured at 12 dominant periods between T$\sim$38-114 s, whereas Love waves are measured at seven dominant periods between T$\sim$38-62 s. We choose to include only shorter-period Love wave measurements (T$\leq$62 s), which have stronger sensitivity to the crust, as can be seen in Figure S2. We performed inversions using longer-period Love waves (T$\sim$69-113 s), which

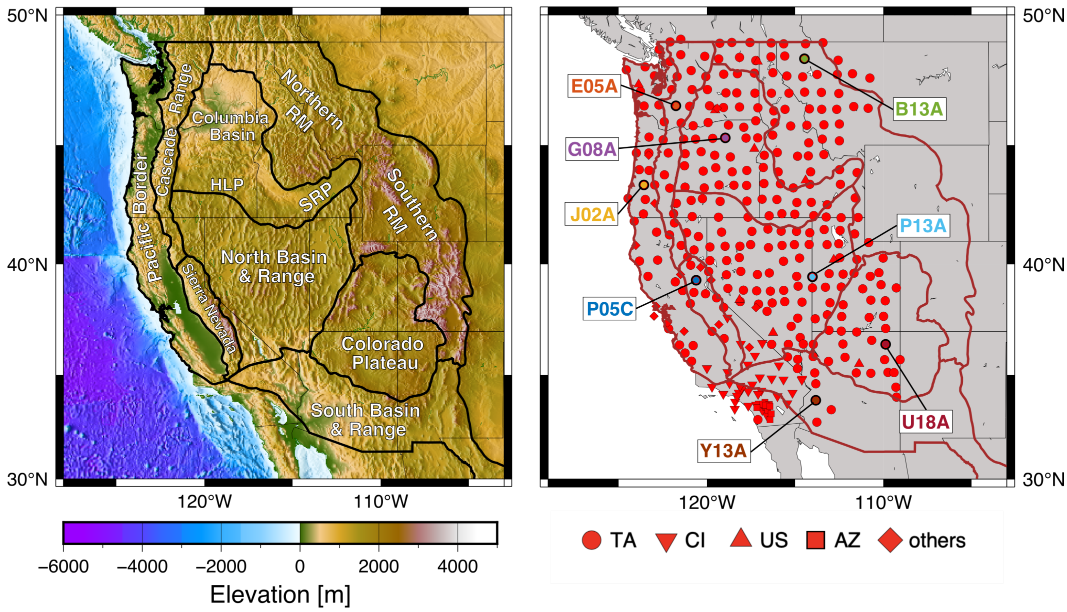

Figure 1. Left: Map of the western U.S., it's major tectonic provinces and other notable features, including the Rocky Mountains (RM), the Snake River Plain (SRP) and High Lava Plains (HLP). The elevation and bathymetry of the region are also plotted, according to ETOPO1. Right: the location of all 351 stations used in this study, with their network represented by different symbol types, as shown in the key. Other networks (diamond symbol) include BK, NN, IU, LB and LI. For each major tectonic province we selected one illustrative station, which is labelled. These eight selected stations are used as illustrative examples throughout this paper. The major tectonic provinces are delineated as solid brown lines.

resulted in very similar 1-D shear-wave speed (v_S) profiles in the crust, thus not affecting the results of this study, but they occasionally led to less stable inversions likely due to noisier measurements. Our measurement procedure provides a total of 6,423 multi-frequency, surface-wave amplification measurements used in this study.

2.2 Measurement technique

We use Rayleigh and Love wave amplification measurements obtained with the measurement technique developed by Schardong et al. (2019), which is briefly summarised in this section. The local frequency-dependent amplification of surface waves at a given receiver, R, is theoretically expressed by (e.g., Ferreira & Woodhouse, 2007):

$$A_R(\omega) = \frac{Y(\omega)}{Y_0(\omega)}\sqrt{\frac{C_g^0(\omega)}{C_g(\omega)}}, \tag{1}$$

where $Y(\omega)$ is the local displacement eigenfunction of the Earth's normal mode equivalent to the surface wave considered at a given frequency ω. $Y(\omega)$ corresponds to the vertical component eigenfunction $U(\omega)$ for Rayleigh waves, and to the transverse component eigenfunction $W(\omega)$ for Love waves. $C_g(\omega)$ is the local group velocity which is measured from spheroidal and toroidal modes for Rayleigh and Love waves, respectively. $Y_0(\omega)$ and $C_g^0(\omega)$ are the corresponding eigenfunction and group velocity, respectively, computed for the 1-D reference model PREM (Dziewonski & Anderson, 1981). The eigenfunctions and group velocities are calculated using a normal mode formalism (F. Gilbert, 1971) and using the software package Mineos 1.0.2 (Masters et al., 2011).

In addition to the amplification (or receiver) contribution $A_R(\omega)$, observed surface wave amplitudes are also affected by source and path effects. Eddy and Ekström (2014) developed a method to remove the contribution from the source and path by averaging ratios of amplitudes between pairs of nearby stations i and j, which is ideally suited to dense seismic networks such as the USArray. Local amplification, $d_{ij}^k(\omega)$, is calculated by taking the ratios of surface-wave amplitudes for a given earthquake, k:

$$d_{ij}^k(\omega) = \ln(A_i(\omega)/A_j(\omega)) = \ln(A_i(\omega)) - \ln(A_j(\omega)) \tag{2}$$

followed by an average taken over all the earthquakes considered. Schardong et al. (2019) followed the same approach, but with some minor modifications considering an azimuthal weighting of the earthquakes,

$$\bar{d}_{ij}(\omega) = \frac{\sum_{k=1}^{N_E} d_{ij}^k w^k}{\sum_{k=1}^{N_E} w^k} \tag{3}$$

The azimuthal weighting coefficient is given by $w^k = 1 - n_E/N_E$, where n_E is the number of earthquakes located in an azimuthal bin of 15°, for each earthquake k, and N_E is the number of common earthquakes recorded at stations i and j. We then calculate the corresponding weighted standard deviation using:

$$\sigma_{ij}(\omega) = \sqrt{\frac{\sum_{k=1}^{N_E} w^k (d_{ij}^k(\omega) - \bar{d}_{ij}(\omega))^2}{\frac{N_E - 1}{N_E} \sum_{k=1}^{N_E} w^k}} \tag{4}$$

We then invert the average inter-station frequency-dependent measurements for local amplification factors at each station ($A_{R,i}$ and $A_{R,j}$). Adopting a least-squares inversion approach, we minimise the misfit function:

$$m^2 = \sum_{ij} \frac{1}{\sigma_{ij}^2} [(\ln(A_{R,i}(\omega)) - \ln(A_{R,j}(\omega)) - \bar{d}_{ij}(\omega)]^2 \tag{5}$$

To constrain the inversion, Schardong et al. (2019) imposed the condition that the sum of the amplification factors must equal the sum of the theoretical amplification factors (Equation 1), calculated using SGLOBE-rani (Chang et al., 2015) for mantle structure combined with CRUST2.0 (Bassin, 2000) for crustal structure.

It was noted in Schardong et al. (2019) that the amplification values obtained with distinct amplification sum constraints vary significantly, which would lead to distinct absolute v_S values when inverting the amplification measurements. Therefore, absolute values of v_S will not be interpreted in this study. However, it was found that inverted v_S perturbations did not strongly depend on the imposed sum of the amplification factors, therefore our model can be interpreted in terms of v_S perturbations.

Inter-station measurement uncertainties, $\underline{\mathbf{e}}_R$, are calculated at all stations and available periods using:

$$\underline{\mathbf{e}}_R = \sqrt{diag(\underline{\underline{\mathbf{P}}}^{\mathbf{-1}} \cdot \underline{\underline{\mathbf{S}}} \cdot (\underline{\underline{\mathbf{P}}}^{\mathbf{-1}})^{\mathbf{T}})} \tag{6}$$

where the $\mathbf{P}$ matrix relates $\ln(A_{R,i}(\omega)) - \ln(A_{R,j}(\omega))$ with $d_{ij}(\omega)$ (Equation 5) and $\underline{\underline{\mathbf{S}}}$ a diagonal matrix containing observed data uncertainties in the form of weighted standard deviations (Equation 4). These errors cannot be directly compared to previous studies (e.g., Lin et al., 2012; Eddy & Ekström, 2014) because of different data error definitions used.

We also apply selection criteria on our amplification curves in order to remove all outliers, for both Rayleigh and Love waves. Specific details are given in the supplementary information of Schardong et al. (2019), and here we briefly summarise them. As shown in Figure S3, we ensure that we only consider amplification factors for which five or more inter-station measurements are available. We ensure there is a good azimuthal coverage of stations around our primary station, in order to avoid azimuthal biases leaking into our inter-station amplification measurements. Specifically, we remove all stations with an azimuthal completeness coefficient of less than 20% (as defined by Equation 2 in the SI of Schardong et al., 2019). Outliers due to geographical coherency are removed by ensuring amplification factors for each station do not vary by more than 2.5σ compared to all nearby stations, where σ is the standard deviation of the amplification values of all nearby stations. Lastly, we remove all stations with a propagated error greater than 0.1, as given by Equation 6. This threshold value ensured obvious outliers were removed, whilst keeping the bulk amount of data available.

In this study we perform inversions of inter-station amplification measurements from 432 stations in the western U.S., which have both Rayleigh and Love amplification data. Following these inversions, we removed stations for which the inversions had a data misfit larger than 20 (Equation 7). Moreover, we visually examined all the stations and removed those that showed rough (i.e., non-smooth) or irregular amplification curves that could not be matched in the inversions. As a result, we kept a total of 351 stations and are still left with a good distribution of stations across the region (Figure 1).

2.3 Results

Figure 2 shows illustrative examples of observed amplification curves for Rayleigh and Love waves compared to theoretical predictions using the 1-D depth profiles from

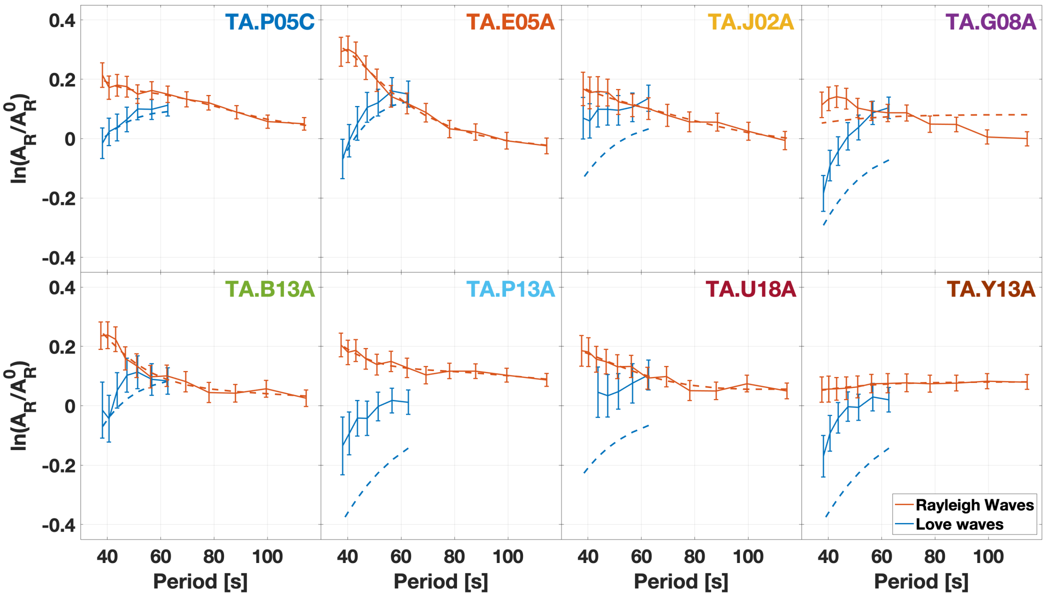

Figure 2. Comparisons of measured (solid lines with error bars) and theoretical amplification curves (dashed lines), calculated using 1-D profiles from SWUS-amp Schardong et al. (2019). Each illustrative station, given in the top-right of each panel, resides in a different major tectonic province (see Figure 1). Amplification curves for Rayleigh waves are shown in red, while for Love waves are shown in blue.

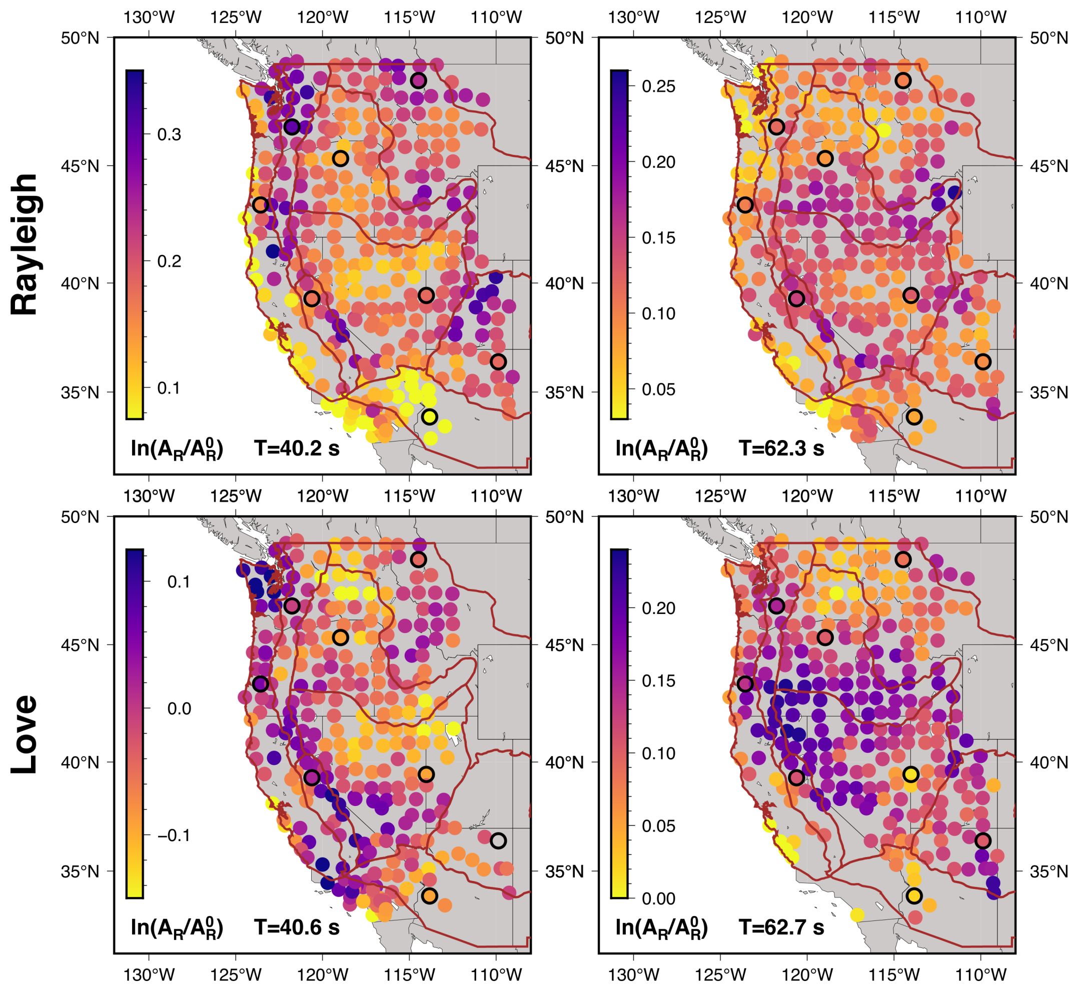

Figure 3. Top row: Rayleigh wave amplification measurements at T∼40 s (left) and T∼62 s (right). Bottom row: Love wave amplification measurements at T∼41 s (left) and T∼63 s (right). The eight illustrative stations shown in Figure 1 are highlighted with black borders. Brown lines outline the major tectonic provinces.

SWUS-amp (Schardong et al., 2019). Each station resides in a different major tectonic province (Figure 1), in order to show the range of amplification curves available in the western U.S. Given that SWUS-amp was built using the same Rayleigh wave dataset as in this study, the fit between the theoretical and observed Rayleigh wave amplification curves is excellent. However, the Love wave theoretical curves show a range of data fits. Whilst stations TA.P05C and TA.E05A show reasonable data fits, other stations show very poor fit, such as TA.U18A and TA.Y13A. Given the strong sensitivity of Love waves to the crust, as can be seen in Figure S2, this suggests that using Love wave amplification may help to constrain a more detailed crustal model than in SWUS-amp.

Figure 3 shows the local amplification measurements obtained for the available stations at wave periods of T∼40 s and T∼62 s. The Rayleigh and Love wave amplification maps look different to one another because of their distinct sensitivities, however there are also some common features. At T∼40 s for Rayleigh waves, low-local amplification is retrieved in the South Basin & Range and along the Pacific coastline. Conversely, high amplifying structures are retrieved along the Sierra Nevada and Cascade ranges, and at the northeastern edge of the Colorado Plateau. At T∼62 s, high amplification is imaged along the southern Columbia Basin and Snake River Plain. This is in contrast with the low-amplifying structures in the along the Pacific border, the North Rocky Mountain and in the northernmost part of the Columbia Basin (see Figure 1 for the geographical location of these regions).

At T∼40 s for Love waves, we observe low-amplifying structures beneath the Columbia Basin and northeastern Basin & Range. Highly-amplifying structures are observed along the northern Pacific coast and the western border of the North Basin & Range. At T∼62 s, there are highly-amplifying structures across the North Basin & Range, the Cascade Range and the southern Columbia Basin. This is in contrast to the northern Columbia Basin, Northern Rockies and southern Pacific border.

Previous studies have shown that local Rayleigh wave amplification shows a correlation with crustal thickness (H. Gilbert, 2012; Eddy & Ekström, 2014). We observe a similar pattern in Figure 3, where the thick crust beneath the Sierra Nevada Mountains, Northern Rocky Mountains and Snake River Plain shows high-amplification, whereas the thinner crust beneath the Columbia Basin, North and South Basin & Range and Pacific coast shows low-amplification. Likewise, the Love wave amplification maps show a similar correlation to crustal thickness.

The propagated amplification errors (Equation 6) can be seen for each station in Figure 4, for the same illustrative wave periods. For both Rayleigh and Love wave amplification error maps, the errors are largest around the edges. The reason for this is because the number of stations pairs is lower for the outer stations (see Figure S3a), and consequently the azimuthal coverage of station pairs is also lower (Figure S3b). Propagated errors are greater for Love waves because in general horizontal component data are noisier than vertical component data.

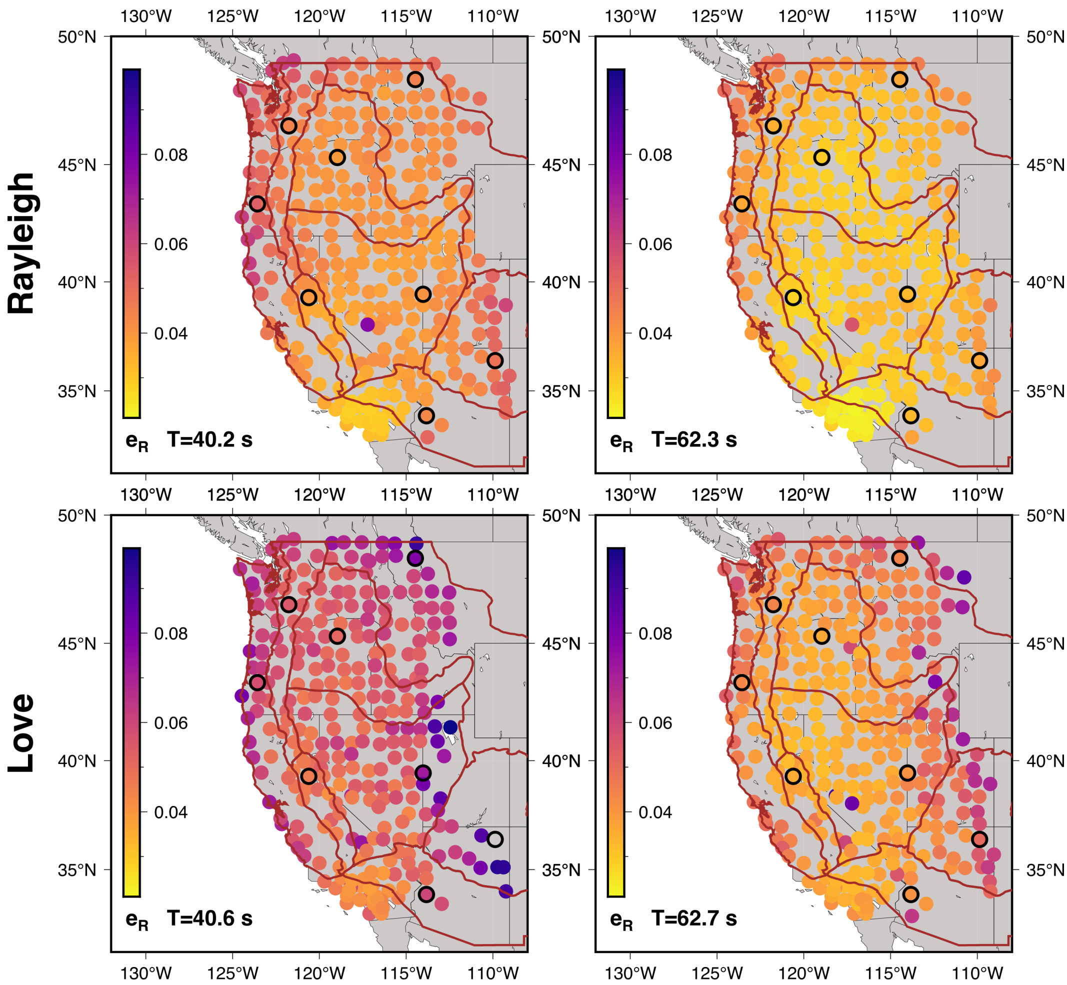

Figure 4. Top row: Rayleigh wave amplification error measurements at T∼40 s (left) and T∼62 s (right). Bottom row: Love wave amplification error measurements at T∼41 s (left) T∼and 63 s (right). The eight illustrative stations are highlighted with black borders. The major tectonic provinces are outlined in solid brown lines.

3 Inverting surface wave amplification for crustal shear wave speed

3.1 Inversion method

There is a non-linear relation between surface-wave amplification and Earth structure. We therefore use the fully non-linear Neighbourhood Algorithm (NA; Sambridge, 1999) to jointly invert the observed amplification curves for depth-dependent v_S beneath each available station. The NA is a Monte Carlo based approach that divides the parameter space into Voronoi cells (Voronoï, 1908) to quickly find an ensemble of models that best fit the data. The NA has been used to constrain crustal structure in a number of different settings, including in the western U.S. (e.g., Moschetti et al., 2010a), Portugal (Attanayake et al., 2017), northern Italy (Berbellini et al., 2017), the Azores (Ferreira et al., 2020), central Java (Ariyanto et al., 2018), the Netherlands (Yudistira et al., 2017) and Greenland (Jones et al., 2021). The NA is composed of two main stages. Firstly, the NA randomly samples the parameter space and each model is ranked according to its misfit between the observed and theoretical amplification curves. Secondly, the NA enters an optimisation stage where in each iteration models are sampled within the neighbourhood of the best-fitting models. After extensive testing, in the initial stage we choose to sample 2,000 random models. Then, in the second stage, for each iteration the NA picks 20 models within the neighbourhood of the best five models from the previous iteration. Moreover, the NA proceeds for 500 iterations to ensure the solution converges on the same model each time. Figure S4 shows an example of misfit evolution, clearly showing good convergence.

We use a L_2-norm misfit function:

$$s(\mathbf{m}) = \sum_{i=1}^{N} \frac{(A_{R,i} - g_i(\mathbf{m}))^2}{e_{R,i}^2} \tag{7}$$

where $g_i(\mathbf{m})$ is the predicted amplification for the model $\mathbf{m}$ being sampled, $A_{R,i}$ is the observed amplification, $e_{R,i}$ is the observed error, N is the number of wave periods and i is the individual wave period.

We ran a number of synthetic tests to verify if the addition of Love wave amplification data helps to further constrain mantle v_S compared to using Rayleigh wave amplification data alone, but extensive testing revealed that due to their strong sensitivity to the crust, they could not constrain the mantle. Next, due to Love wave amplification being mainly sensitive to v_{SH}, we performed joint inversions of Rayleigh and Love wave amplification data for a radially anisotropic crust, but the increased number of parameters that needed to be inverted for with a relatively small dataset led to unstable inversions. Hence, we invert for an isotropic crust, and have verified that the data fit is good for both Love and Rayleigh wave data (i.e., we ensured that the data used in this study do not require radial anisotropy). Given that crustal layers typically have strong contrasts in seismic properties and the success of previous studies in using layered parameterisations for the crust, notably with three layers (e.g., Laske et al., 2012; Schmandt et al., 2015; Ferreira et al., 2020), we decided to also use a three-layered crustal parameterisation. Since our mantle model SWUS-amp (Schardong et al., 2019) was successfully built using Moho depths from CRUST1.0, we also constrain the depths of our three-layer crustal model using CRUST1.0 (Figure S5). We choose not to invert for sediment layers, as that would require shorter period amplification measurements.

One of the advantages of using the NA is that it provides an ensemble of models that can be used to estimate uncertainties for our final solution. We calculate the percentual uncertainty e_{v_s} for each station used to build our model by considering the range of velocities, $v_{s,\max}-v_{s,\min}$, of all models within a 20% misfit of the best-fitting model, $v_{s,\text{best}}$, in each crustal layer.

$$e_{v_s} = \frac{(v_{s,\max} - v_{s,\min})}{v_{s,\text{best}}} \times 100 \tag{8}$$

We choose a threshold of 20% because it includes models that fit the amplification curves reasonably well. A looser threshold would include models with a poor data fit, and a stricter threshold would not be representative of the range of models that fit the data relatively well.

We invert for v_S whilst scaling for v_P and ρ using the general Brocher relation (Brocher, 2005). The mantle structure is fixed to that of SWUS-amp (Schardong et al., 2019) between the Moho and ~300 km depth and to PREM beneath this depth. In the next section we will justify this choice of mantle model with the help of synthetic inversion tests and trade-off tests between crustal and mantle structure. Constraints are imposed on the inversion whereby v_S must increase with depth within each crustal layer as well as beneath the Moho. Previous crustal models in the western U.S. show that v_S always increases with depth within these ranges (e.g., Schmandt et al., 2015; Shen & Ritzwoller, 2016) and our inversion tests showed that these constraints help stabilise the inversions.

We invert for shear-wave velocity perturbations ($\frac{\delta v_S}{v_S}$), with respect to the average crustal v_S of PREM. In order to search a wide range of possible model parameters, we allow the inversion to search between ±40% of the average crustal v_S of PREM in each layer.

3.2 Synthetic inversion tests

We perform synthetic inversion tests to investigate how capable our inversion method is of retrieving realistic input crustal models. We use the results from our best real data inversion model as our input model, in order to perform the tests on realistic models. Gaussian random noise is added to each data point by simulating 200 predicted amplification curves using the standard deviations of the real data measurements. The average amplification curve and standard deviation of these simulated curves are used as the input synthetic data into the NA as described in section 3.1.

Figure 5 shows the results from synthetic inversions for our 8 stations of interest. Overall, the synthetic inversions work very well, showing that the NA converges to the input model even with noise introduced. Models within a 20% misfit of the best retrieved model are shown by coloured lines and it is encouraging to see that these models show a small range in velocities, centred around the best-fitting model. There are, however, some slightly imperfect solutions which are due to trade-offs in v_S between the crustal layers (e.g., for stations TA.P05C and TA.G08A).

In order to investigate model parameter trade-offs in our inversions further, we produce trade-off plots by plotting all the crustal and mantle model parameters used in the inversions against each other (see e.g., Figure S6 for station TA.Y13A). Furthermore, we perform inversions inverting not only for the three crustal layers but also for the v_S coefficients of one spline function describing the uppermost mantle structure between the Moho and ~90 km depth. This ensures that we are not biasing our crustal model by fixing the mantle to SWUS-amp. Figure S7 in the supplementary information shows that there is a small trade-off in v_S between the uppermost mantle and lower crust, indicating that fixing v_S in the mantle does not significantly affect the retrieved crustal model. This also highlights the fact that Love waves have low sensitivity to the uppermost mantle, but add important sensitivity to the crust, as can be seen by the sharp gradient in sensitivity in Figure S2. Conversely, Rayleigh waves show strong sensitivity to the crust

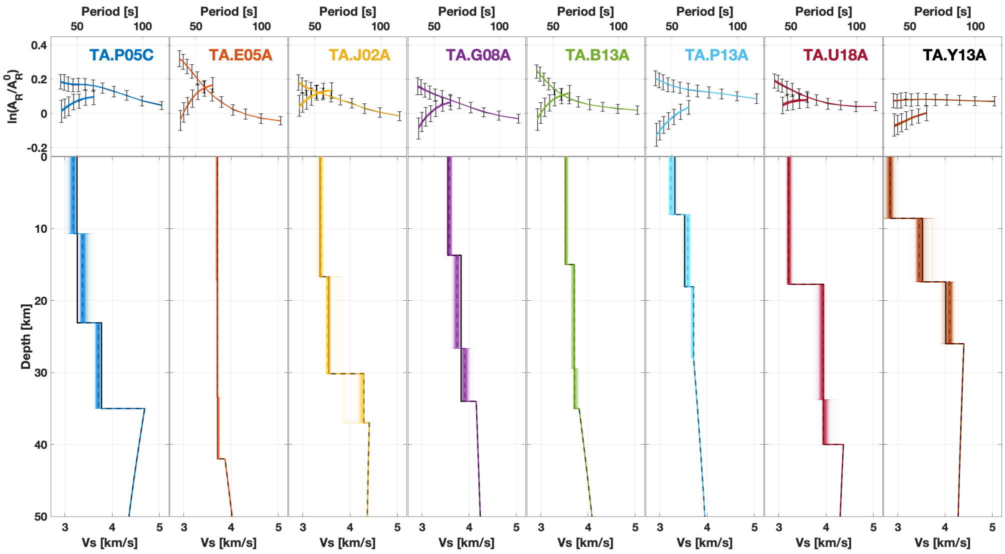

Figure 5. Example of results from synthetic inversion tests. Top row: amplification curves computed for synthetic input 1-D v_S profiles (black lines with error bars) and the retrieved output 1-D v_S profiles (coloured lines). The curves with longer periods are for Rayleigh waves, and the shorter curves are for Love waves. Bottom row: Corresponding input (black dashed lines) and output (bold coloured lines) v_S models. The more transparent coloured lines show the models with misfit values within 20% of the model with the lowest misfit.

and uppermost mantle, but, as found by Schardong et al. (2019), they cannot constrain alone crustal models more complex than a single layer.

3.3 Results from real data inversions

We jointly invert Rayleigh and Love wave amplification curves for 1-D v_S profiles using the NA as described in Section 3.1. Figure 6 shows examples of 1-D v_S profiles obtained for the eight illustrative stations located within each major tectonic province in the western U.S considered in this study. For reference, we compare our model with the layered crustal model of Schmandt et al. (2015) and the smooth crustal model of Shen and Ritzwoller (2016), which were built using completely independent data sets from this study. As with the synthetic profiles in Figure 5, we plot all models with a data misfit within 20% of the best-fitting model. These models are clustered around the best-fitting model, showing that we have a well-converged solution and that any trade-offs appar-

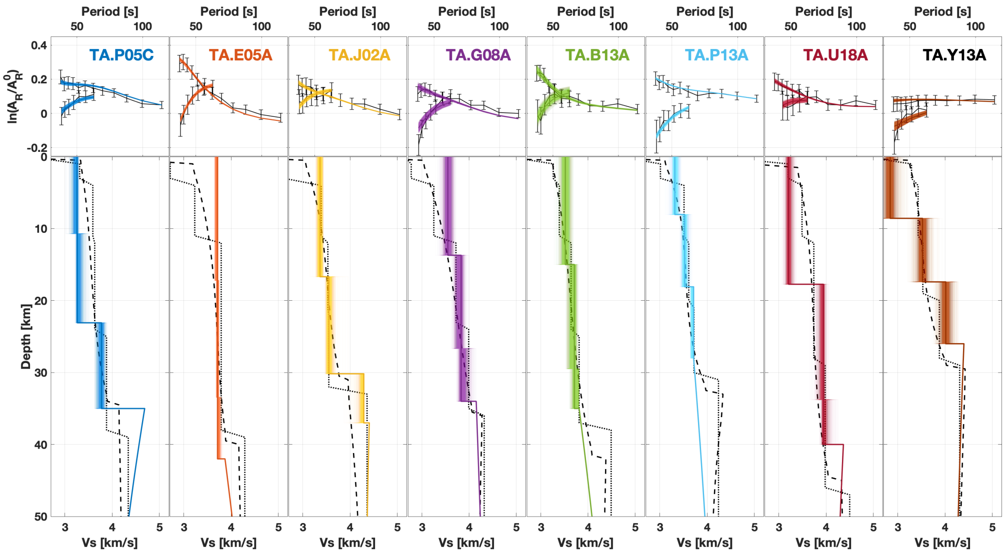

Figure 6. Real data inversions for depth-dependent v_S for the eight example stations located in each major tectonic province in the western U.S. (see Figure 1). Top row: Amplification curves for Rayleigh waves (long curves) and Love waves (short curves) for real data (black lines with error bars), the best retrieved model (thick coloured lines) and models within a 20% misfit value of the best-fitting model (thin coloured lines). Bottom row: 1-D shear-velocity crustal profiles for SWUS-crust (coloured lines), compared to the models of Schmandt et al. (2015) (dotted lines) and Shen and Ritzwoller (2016) (dashed lines).

ent in the model do not have a significant impact on our final model. Figure S4 shows an illustrative example of convergence of an inversion for station TA.P13A. It can be seen that convergence is achieved after 10,000 models but we continue the inversion up to 12,000 models for insurance.

We compare SWUS-crust to the single crustal layer of SWUS-amp (Figure S1) to further check if our modelling is biased by the presence of anisotropy. Similar crustal features are seen in SWUS-amp compared to SWUS-crust, for example high v_S beneath the Columbia basin, Colorado Plateau and Northern Rocky mountains. Similarly, low v_S is observed beneath parts of the Northern Basin & Range and the High Lava Plains. Such similarities suggest that the inclusion of Love wave amplification data in SWUS-amp has not introduced a bias due, e.g., to radial anisotropy. Furthermore, as mentioned previously, SWUS-amp does not fit Love wave data well, as seen in Figure 2. We ran several anisotropic and isotropic inversions including Love waves and whilst isotropic inversions remained robust, anisotropic inversions were not. The data fit for both Rayleigh and Love waves is good, but is not always perfect, indicating that a small amount of anisotropy could be present, and indicating no clear bias. Future robust modelling of crustal anisotropy requires the inclusion of further data types such as, e.g., dispersion data.

There are similarities and differences between the various 1-D v_S profiles. We notice that our results obtained for the lower- and mid-crustal layer match the other models well, but there are some differences in the upper-crustal layer. In some profiles we observe higher upper-crustal v_S values (e.g., for stations TA. E05A, TA.G08A) and in other cases we observe lower upper-crustal v_S (e.g., TA.U18A, TA.Y13A). The geographical differences in the velocities and the model uncertainties will be discussed in detail in the next section.

The 1-D v_S profiles are interpolated laterally for each layer using an ordinary kriging routine to obtain a new 3-D crustal model in the western U.S. This technique was successfully used in previous imaging studies (e.g., Berbellini et al., 2017; Schardong et al., 2019; Jones et al., 2021), as the technique allows for interpolation of sparse or irregularly sampled data.

In order to estimate the spatial covariance amongst our stations, we first constructed a semi-variogram. This quantifies the degree of variability in the inferred velocities as a function of the separation distance. A "spherical model" is used to quantify the increase in variability with increased separation distance. The extracted parameters from the semi-variogram describing how the velocities at stations covary with separation distance are used to model the covariance between velocities at stations and velocities across a uniform grid.

We explore a range of models to fit the semi-variogram (for example in the upper crustal layer, Figure S8), and choose a spherical model as it both fits the semi-variogram well and shows relatively low interpolation uncertainty. We note that, as expected, uncertainties in the interpolated values decrease in areas with high station coverage. Figure 7 shows the model before and after interpolating the profiles. We refer to the resulting model as SWUS-crust, whose key features will be discussed in the next section. For completeness, we also show SWUS-amp in terms of absolute v_S in Figure S9.

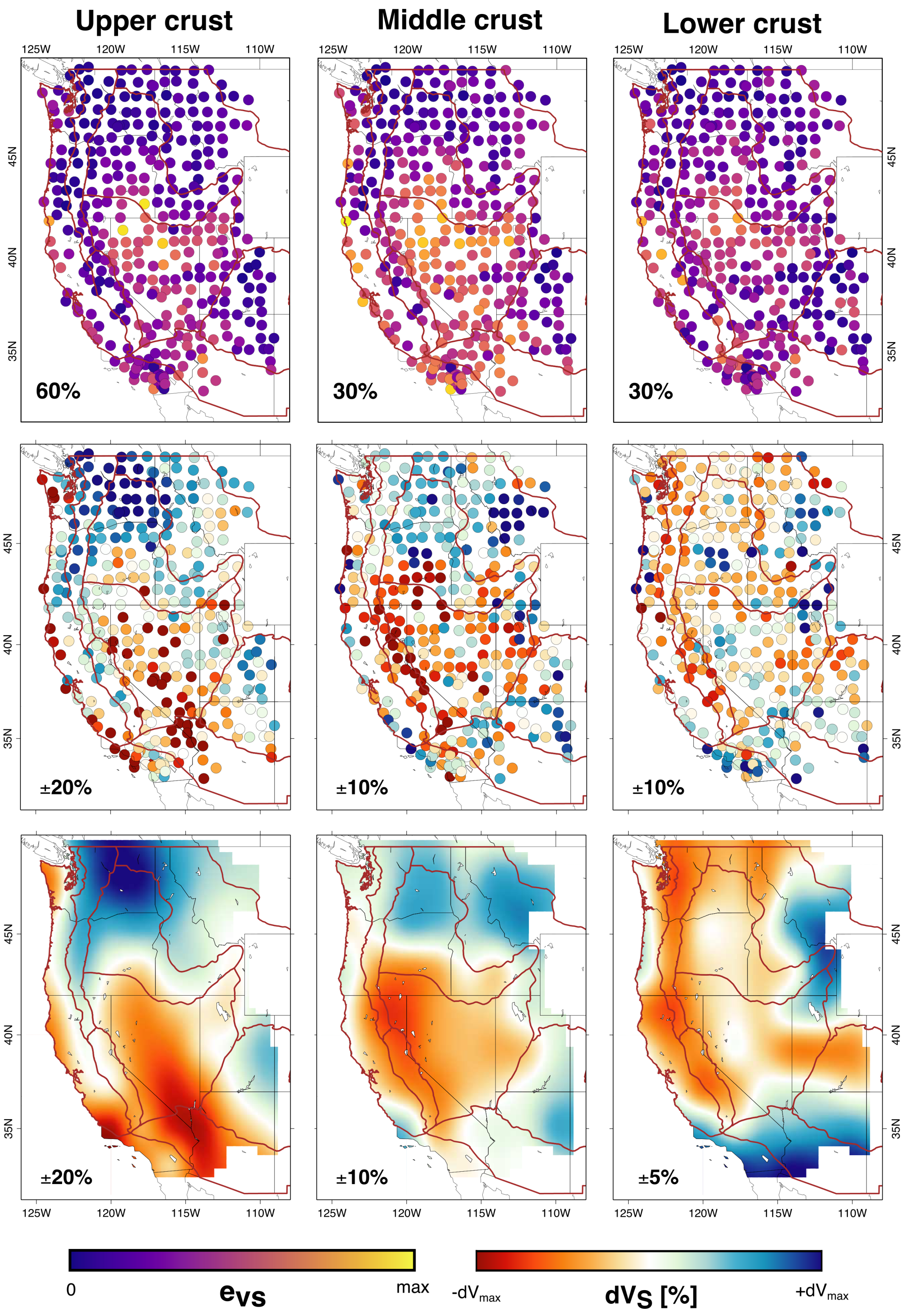

Figure 7. Tow row: Maps of percentual model uncertainties, as defined by Equation 8, for each station used in the construction of SWUS-crust. The maximum of the scale bar is indicated in the bottom left of each panel. Middle row: Deviations from the average v_S in each layer, in the upper, middle and lower crust at each station for our model SWUS-crust. Bottom row: the same as the top row but after kriging interpolation (see text for further details).

Figure 7 also shows the uncertainty of our real data inversions in each crustal layer, as defined by Equation 8. There appears to be a relation between crustal thickness and model uncertainty, whereby the regions of thinnest crust (e.g., North and South Basin & Range, Pacific Coast) have the highest uncertainty. The crustal thickness in CRUST1.0, in general, is shallower than in Shen and Ritzwoller (2016), who used receiver functions to help constrain the Moho depth, as can be seen in Figures 5 and 6. As a result, we re-ran our inversions changing the Moho depth to that defined by Shen and Ritzwoller (2016) for four stations in the North Basin & Range, as seen in Figure S6. Uncertainty in the lower crust decreased by $\sim$3%, which is not very substantial. This suggests that uncertainties in Moho depth defined by CRUST1.0 do not significantly affect the uncertainty in our model. Model uncertainties in the upper crust are generally higher compared to the middle and lower crust. This is likely due to the fact that we do not invert very short period data, which would be most sensitive to upper crustal depths.

4 Discussion

Previous studies of the crustal structure of the western U.S. have used various combinations of data, including surface wave dispersion data from both seismic ambient noise and teleseismic events, Rayleigh wave ellipticity measurements and receiver functions. In this study we built the first crustal model based on Rayleigh and Love amplification data alone with wave periods T>38 s. As shown by the synthetic tests presented in section 3.2, the narrow depth sensitivity of these observables (Figure S2) enables the construction of our new detailed crustal model of the western U.S., SWUS-crust.

4.1 Comparison with other models

Table S1 in the Supporting Information provides details on the data sets, parameterisation, forward modelling, inversion methods and constraints used by other models discussed in this study; Laske et al. (2012); Moschetti et al. (2010a); Schmandt et al. (2015); Shen and Ritzwoller (2016); Porter et al. (2016); Xie et al. (2018); Chai et al. (2015).

Figure 8 compares SWUS-crust with other crustal layered models of the western U.S., including the global crustal model CRUST1.0 (Laske et al., 2012), the regional models of Moschetti et al. (2010a) and Schmandt et al. (2015). Whilst we do not invert for sedimentary layers, we choose to show them for the other models to aid our interpreta-

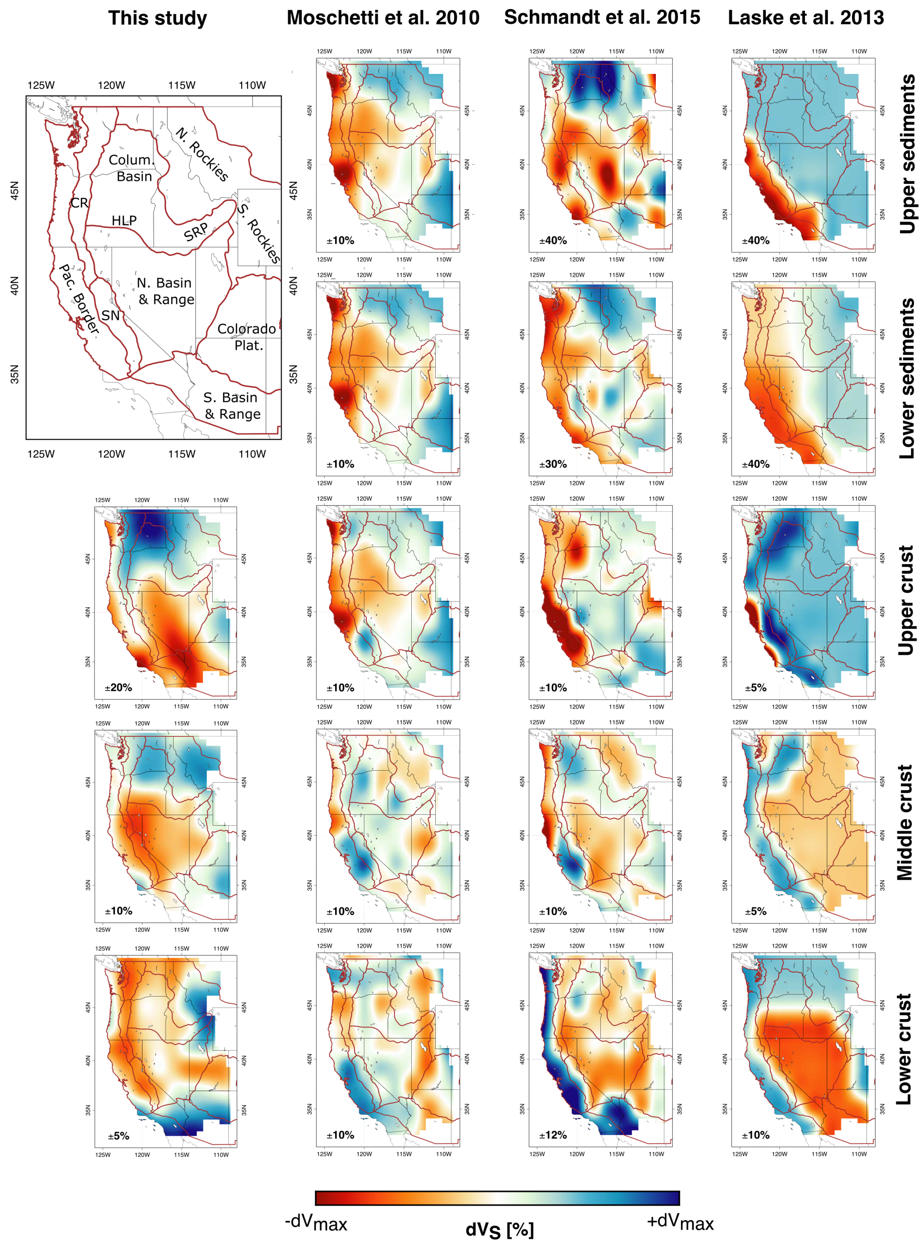

Figure 8. Comparison of the SWUS-crust v_S model (first column) with other layered crustal models, the model of Moschetti et al. (2010a), US-CrustVs-2015 (Schmandt et al., 2015) and CRUST1.0 (Laske et al., 2012). SWUS-crust does not constrain sedimentary layers, hence there are missing panels. In their place is a map showing the location of key tectonic features that are discussed. For each map, the velocity perturbations are presented with respect to the average velocity of that map. The limits of the perturbations are given in the bottom-left of each map and the boundaries of each tectonic province are shown by brown lines.

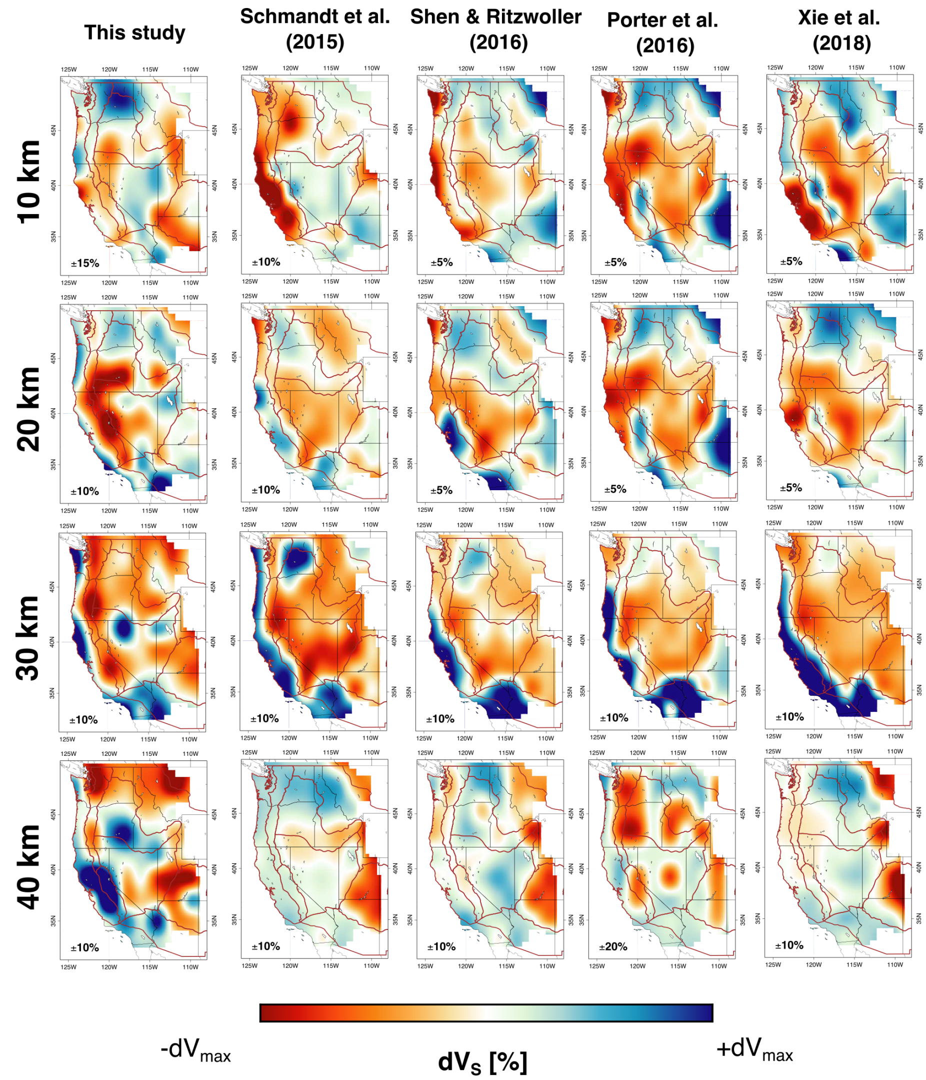

Figure 9. Comparison of the SWUS-crust (first column) with other local tomographic models; Schmandt et al. (2015); Shen and Ritzwoller (2016), Porter et al. (2016) and Xie et al. (2018) at depths of 10, 20, 30 and 40 km. The velocity perturbations of all models are expressed with respect to the average velocity at each depth respectively. The bounds of the colour scale are shown in the bottom-left of each map and the boundaries of each tectonic province are shown by brown lines. The lateral borders of SWUS-crust is also added to each model in order to aid in their comparisons.

tion, since the upper crust layer of SWUS-crust may also reflect shallower sedimentary structures. In addition to these models, we also compare SWUS-crust to a number of smoothly parameterised crustal models at depth intervals of 10 km, (Figure 9) Shen and Ritzwoller (2016); Porter et al. (2016); Xie et al. (2018) and intervals of 5 km for further models in Figure S10 (Chai et al., 2015).

Figures 7 and 8 show that there are some similarities between the different models, notably between the models with a layered parameterisation shown in Figure 8, which show for example mostly low crustal v_S anomalies along the Pacific coast in the upper crust and high crustal v_S anomalies beneath the Columbia basin in the middle crust. On the other hand, there are also considerable differences between the models, notably regarding their small scale structures. For example, SWUS-crust shows a lot of regional variations compared to CRUST1.0 (Figure 8) and the model of Chai et al. (2015) (Figure S10), while other models show more comparable small-scale heterogeneity.

4.2 The Northern Rockies, the Columbia basin and High Lava Plains

Figures 7 and 8 show that SWUS-crust images a high v_S anomaly in the upper and middle crust beneath the Northern Rocky mountains, but a slower anomaly in the lower crust. Specifically, at 10 and 15 km depths in Figure S10, the Northern Rockies are underlain by low v_S anomalies, largely matching other models at these depths (e.g., Schmandt et al., 2015; Laske et al., 2013; Chai et al., 2015). This could be explained by intense magmatism during the Cenozoic, prior to uplift in the region (Tesauro et al., 2014). There is little consistency between models in the middle and lower crust beneath this region (Figure 8; see also the differences e.g., at depth slices of 20 and 35 km in Figure S10).

Figure 8 shows that the signature of the Columbia basin in SWUS-crust is a high v_S anomaly throughout the upper and middle crust, with its magnitude decreasing strongly with depth. A similar trend is observed in all models, with the exception of Schmandt et al. (2015) and Moschetti et al. (2010a) which show low v_S anomalies in the upper crust. This anomaly could be related to a mafic composition following continental rifting during the initiation of the Cascadia subduction zone (Catchings & Mooney, 1988b; Schmandt & Humphreys, 2011). It is worth noting that, as explained previously, we do not invert for sediment layers as they are too thin to be constrained by our data, which have a minimum period of 38 s. Therefore care must be taken when comparing our model with others at shallow depths (e.g., 5-10 km), the depths at which other models image sediments, while our images may show a mix of sediments and other deeper structures (Figure 9 and S10). For example, the Columbia basin is covered by a thick layer of Miocene flood basalts (Catchings & Mooney, 1988b, 1988a) which we might have imaged in the upper crustal layer. This anomaly is similarly reflected in the upper sediments of Schmandt et al. (2015).

In order to further explore the differences observed beneath the Columbia basin between our model and the model of Schmandt et al. (2015), we computed theoretical amplification curves for the input model of Schmandt et al. (2015) at the points of the model nearest to nine illustrative stations shown in Figure S11. The same test was performed using the model made by Shen and Ritzwoller (2016), as shown in Figure S12. These two models show the Columbia basin, in particular the Yakima Fold Belt in the western part of the basin, as largely a low-velocity anomaly in the upper crust. Therefore we ran a test to see if these models fit our observations. Forward modelling of these models shows that neither fits all data particularly well (Figures S11, S12). The model of Shen and Ritzwoller (2016) fits the Love wave amplification curves well, but not the Rayleigh wave curves at short periods (T $\sim$35-70 s). In contrast, the model of Schmandt et al. (2015) fits the Rayleigh wave data rather well, but not the Love wave data. This test helps us to confirm that the surface wave amplification data require the observed fast v_S anomaly and that this anomaly is not due e.g., to the model parameterisation chosen. Both models use similar data types, so the observed differences could be due to their choice of inversion scheme.

The High Lava Plains (HLP in Figure 8), located in central Oregon, form a boundary between the Basin & Range province to the south and the Columbia basin to the north. This is also represented in Figure 8, where the HLP divide the high v_S anomalies of the Columbia basin with the low v_S anomalies of the North Basin & Range. In all layers of SWUS-crust, low v_S anomalies are observed beneath the HLP and the northern border is particularly well delineated in the middle crustal layer. The plains are also well delineated in CRUST1.0 but not in its upper crustal layer, while Moschetti et al. (2010a) only observed this low v_S anomaly in the upper crust. The anomaly observed in SWUS-crust throughout the entire crust may be explained by a magma injection due to recent volcanism along the Yellowstone hotspot track (Jordan et al., 2004).

4.3 The Pacific coast, the Cascade range and Snake River Plain

SWUS-crust shows low v_S anomalies in the upper crust beneath the Pacific coast (Figure 8), similarly to other models, and high v_S anomalies between 20-40 km depth (Figure 9 and Figure S10), which may reflect mafic material formed by accreted oceanic crust (Lin et al., 2014). SWUS-crust does not show a clear anomaly beneath the Great Valley in California, unlike the clear observation in the middle crust in the models of Moschetti et al. (2010a) and Schmandt et al. (2015). However, when studying the station distribution in Figure 7, there is a clear lack of stations considered in the valley.

In the Cascade range, we observe high v_S anomalies in the upper crust underlain by a neutral v_S anomaly in the middle crust and a low v_S anomaly in the lower crust. No clear trend is observed beneath the Cascade range in Figure 8, but it remains a consistently low v_S anomaly at 30 km depth in Figure 9, and at 35 km depth in Figure S10, with the exception of Laske et al. (2012). Low velocities at lower crustal depths may reflect crustal thickening and/or warm mantle temperatures (Chai et al., 2015).

To the east, the Snake River Plain (SRP) is not associated with a continuous velocity anomaly region in our model, but instead shows several distinct anomalous features. In the upper crust the region shows high to low v_S anomalies from west to east, but the opposite is observed in the middle and lower crust. This could be related to more recent volcanism towards Yellowstone and to the intrusion of mafic material (Sparlin et al., 1982). In contrast, the models of Moschetti et al. (2010a) and Schmandt et al. (2015) do not show any clear crustal velocity anomalies along the SRP, with the exception of the lower crust, where there is a slow v_S anomaly at the end of the hotspot track towards Yellowstone. However, when looking at the depth slices in Figure 9, the majority of models show low, or neutral v_S anomalies at 20-30 km depth. Stronger low v_S anomalies furthest east of the SRP at 30-40km in Figure 9 may be due to a partially melted, hot body of granitic composition (Smith et al., 1982).

4.4 The North Basin and Range, the Sierra Nevada and the Colorado Plateau

The North Basin and Range appears largely as a low v_S anomaly throughout SWUS-crust (Figures 7 and 8). Most models show a similar feature, although at 10 km depth in Figure 9, large portions of the North Basin and Range show high v_S anomalies, in agreement with the model of Schmandt et al. (2015). Low v_S anomalies are consistent across all models in Figure 8 in the middle crust and between 20-30 km depth in Figure 9. This is with the exception of the thinnest parts of the North Basin and Range (see Figure S5) at the northern border. Low v_S anomalies in the middle crust may be related to extensional deformation, as Moschetti et al. (2010b) imaged strong crustal anisotropy in this region. In the lower crust, low v_S anomalies may reflect Quaternary volcanism (Walker et al., 2004) and more recent intrusion of melts into the lower crust (Lin et al., 2014), which may produce an area of high heat flow (Tesauro et al., 2014).

The nearby Sierra Nevada mountain range does not seem to be associated with clear, well defined anomalies in SWUS-crust, but shows a neutral v_S anomaly in the upper crust, which changes to a low v_S anomaly in the middle and lower crust. A few models, such as that of Moschetti et al. (2010a), Schmandt et al. (2015) and Laske et al. (2012) show the Sierra Nevada as a more neutral feature, especially in the mid and lower crustal layers. In these models, the Sierra Nevada dissects the high v_S anomalies of the Pacific coast and Great Valley to the west, and the low v_S anomalies of the North Basin & Range to the east (see Figures 8 and 9).

Finally, the Colorado Plateau shows a largely high v_S anomaly in the upper and middle crust, generally agreeing with most other models in Figure 8, with the notable exception being the middle crust in CRUST1.0 (Laske et al., 2012). The fast v_S anomalies observed in this region may be attributed to the mafic composition of the plateau as discussed, e.g., by Zandt et al. (1995). In addition, higher v_S anomalies in the centre of the plateau compared to the boundaries in the upper crust may be related to cold temperatures, which is consistent with low heat flow measurements in the region (Blackwell & Richards, 2004). Figures 9 and S10 show that at lower crustal depths (>25 km) the plateau is largely associated with a low v_S anomaly, matching almost all other models. As discussed by Moschetti et al. (2010a), it remains unclear if this is due to thermal or compositional effects.

4.5 Limitations and future work

While this work showed that crustal structure can be constrained by surface wave amplification data alone, the use of shorter period data is needed to image smaller-scale structures. For example, in order to invert for thin sedimentary layers, we could include ambient noise and ellipticity measurements to add sensitivity to the top few kilometers of the crust. Moreover, future joint inversions of amplification data along with surface wave dispersion measurements and receiver functions would help to further constrain v_S in the crust, and also the depths of the crustal layers. This may also help to improve the data fit, particularly for seismic stations in the North Basin and Range, as the layer depths will no longer have to be fixed to CRUST1.0. Finally, while thanks to a careful data selection we could fit both Rayleigh and Love wave amplification data well, by incorporating further data types (dispersion, etc), in the future we may be able to constrain anisotropy in the mantle and crust. In turn, this could help significantly to interpret the model in terms of the tectonic and geodynamical evolution of the region.

5 Conclusions

We presented SWUS-crust, a crustal model of the western U.S. built with Rayleigh (T$\sim$ 38-115 s) and Love (T$\sim$ 38-63 s) wave amplification measurements. This is, to the best of our knowledge, the first time Love wave amplification measurements have been used to construct a seismic model. Love wave amplification measurements show a strong sensitivity to the crust and, when jointly inverted with Rayleigh wave amplification data using the Neighbourhood Algorithm, lead to a crustal model that is more detailed than its predecessor model, SWUS-amp (Schardong et al., 2019).

Due to its complex tectonic history, significant variability in shear-wave velocity is imaged across the western U.S. SWUS-crust clearly shows the fast Columbia basin in the upper and middle crust. Moreover, it shows distinct changes in velocity beneath the Colorado Plateau from generally high anomalies in the upper and mid crust, to lower anomalies in the lower crust, particularly at 30 km depth. We largely image the slow North Basin & Range throughout the whole crust. The High Lava Plains of central and southeastern Oregon are imaged in finer detail compared to previous models. In particular, the northern border of the HLP in southern Oregon appears very well delineated in the middle layer of SWUS-crust.

6 Open Research

The surface wave amplification dataset used in this study is attributed to Schardong et al. (2022). The Neighbourhood Algorithm (Sambridge, 1999) can be downloaded from `http://iearth.edu.au/codes/NA/`. The normal mode package used in this study is Mineos 1.0.2 (Masters et al., 2011) published under the GPL2 license. We thank the Computational Infrastructure for Geodynamics (`http://geodynamics.org`) which is funded by the National Science Foundation under awards EAR-0949446 and EAR-1550901. The other tomography models used in this study were obtained from the IRIS Earth Model Collaboration (`http://ds.iris.edu/ds/products/emc-earthmodels/`). ETOPO1 was downloaded from `https://www.ngdc.noaa.gov/mgg/global/`. All maps were built using using Generic Mapping Tools software (Wessel & Smith, 1998).

Acknowledgments

We thank Matthew Fox for fruitful discussion and for his insight into the kriging analysis. We also thank Eric Debayle and David Dobson for fruitful discussion. WS was supported by NERC grant number NE/L002485/1. We gratefully acknowledge the availability of global seismograms from the IRIS Data Services and the IU, II, GEOFON and GEOSCOPE networks. The seismic data analyses and inversions were carried out on the High Performance Computing Clusters Grace and Kathleen, supported by the Research and Computing Support services at UCL. We thank Hendrik van Heijst for providing his surface wave amplitude measurements.

References

Ariyanto, P., Rosid, S., Anggono, T., Januarti, Y., et al. (2018). Crustal structure in the southern part of central java based on analysis of tele-seismic receiver function using a neighbourhood algorithm. In *Journal of physics: Conference series* (Vol. 985, p. 012018).

Attanayake, J., Ferreira, A. M., Berbellini, A., & Morelli, A. (2017). Crustal structure beneath portugal from teleseismic rayleigh wave ellipticity. *Tectonophysics*, *712*, 344–361.

Bao, X., Dalton, C. A., & Ritsema, J. (2016). Effects of elastic focusing on global models of rayleigh wave attenuation. *Geophysical Supplements to the Monthly Notices of the Royal Astronomical Society*, *207*(2), 1062–1079.

Bassin, C. (2000). The current limits of resolution for surface wave tomography in north america. *EOS Trans. AGU. 81: Fall Meet. Suppl., Abstract*.

Bateman, P. C., & Eaton, J. P. (1967). Sierra nevada batholith: The batholith was generated within a synclinorium. *Science*, *158*(3807), 1407–1417.

Bensen, G., Ritzwoller, M., & Yang, Y. (2009). A 3-d shear velocity model of the crust and uppermost mantle beneath the united states from ambient seismic noise. *Geophysical Journal International*, *177*(3), 1177–1196.

Berbellini, A., Morelli, A., & Ferreira, A. M. (2017). Crustal structure of northern italy from the ellipticity of rayleigh waves. *Physics of the Earth and Planetary Interiors*, *265*, 1–14.

Blackwell, D., & Richards, M. (2004). Geothermal map of north america. american association of petroleum geologist (aapg), 1 sheet, scale 1: 6,500,000. *Search in*.

Braile, L., Hinze, W., Von Frese, R., & Keller, G. R. (1989). Seismic properties of the crust and uppermost mantle of the conterminous united states and adjacent canada. *Geological Society of America Memoirs*, *172*, 655–680.

Brocher, T. M. (2005). Empirical relations between elastic wavespeeds and density in the earth's crust. *Bulletin of the seismological Society of America*, *95*(6), 2081–2092.

Buehler, J., & Shearer, P. (2012). Localized imaging of the uppermost mantle with usarray pn data. *Journal of Geophysical Research: Solid Earth*, *117*(B9).

Catchings, R., & Mooney, W. (1988b). Crustal structure of the columbia plateau: Evidence for continental rifting. *Journal of Geophysical Research: Solid Earth*, *93*(B1), 459–474.

Catchings, R., & Mooney, W. D. (1988a). Crustal structure of east central oregon: Relation between newberry volcano and regional crustal structure. *Journal of Geophysical Research: Solid Earth*, *93*(B9), 10081–10094.

Chai, C., Ammon, C. J., Maceira, M., & Herrmann, R. B. (2015). Inverting interpolated receiver functions with surface wave dispersion and gravity: Application to the western us and adjacent canada and mexico. *Geophysical Research Letters*, *42*(11), 4359–4366.

Chang, S.-J., Ferreira, A. M., Ritsema, J., van Heijst, H. J., & Woodhouse, J. H. (2015). Joint inversion for global isotropic and radially anisotropic mantle structure including crustal thickness perturbations. *Journal of Geophysical Research: Solid Earth*, *120*(6), 4278–4300.

Christensen, N. I., & Mooney, W. D. (1995). Seismic velocity structure and composition of the continental crust: A global view. *Journal of Geophysical Research:*

Solid Earth, *100*(B6), 9761–9788.

Christiansen, R. L., Foulger, G., & Evans, J. R. (2002). Upper-mantle origin of the yellowstone hotspot. *Geological Society of America Bulletin*, *114*(10), 1245–1256.

Dalton, C. A., Bao, X., & Ma, Z. (2017). The thermal structure of cratonic lithosphere from global rayleigh wave attenuation. *Earth and Planetary Science Letters*, *457*, 250–262.

Dziewonski, A. M., & Anderson, D. L. (1981). Preliminary reference earth model. *Physics of the earth and planetary interiors*, *25*(4), 297–356.

Eddy, C. L., & Ekström, G. (2014). Local amplification of rayleigh waves in the continental united states observed on the usarray. *Earth and Planetary Science Letters*, *402*, 50–57.

Ferreira, A. M., Marignier, A., Attanayake, J., Frietsch, M., & Berbellini, A. (2020). Crustal structure of the azores archipelago from rayleigh wave ellipticity data. *Geophysical Journal International*, *221*(2), 1232–1247.

Ferreira, A. M., & Woodhouse, J. H. (2007). Observations of long period rayleigh wave ellipticity. *Geophysical Journal International*, *169*(1), 161–169.

Ferreira, A. M., Woodhouse, J. H., Visser, K., & Trampert, J. (2010). On the robustness of global radially anisotropic surface wave tomography. *Journal of Geophysical Research: Solid Earth*, *115*(B4).

Frietsch, M., Ferreira, A. M., & Funning, G. J. (2021). Data-driven two-fault modeling of the mw 6.0 2008 wells, nevada earthquake suggests a listric fault rupture. *Journal of Geophysical Research: Solid Earth*, *126*(4), e2020JB020263.

Gilbert, F. (1971). Excitation of the normal modes of the earth by earthquake sources. *Geophysical Journal International*, *22*(2), 223–226.

Gilbert, H. (2012). Crustal structure and signatures of recent tectonism as influenced by ancient terranes in the western united states. *Geosphere*, *8*(1), 141–157.

Hildreth, W. (2007). *Quaternary magmatism in the cascades: Geologic perspectives.* US Geological Survey.

Huber, N. K. (1981). Amount and timing of late cenozoic uplift and tilt of the central sierra nevada, california; evidence from the upper san joaquin river basin.

Humphreys, E. D., & Coblentz, D. D. (2007). North american dynamics and western us tectonics. *Reviews of Geophysics*, *45*(3).

Jones, G. A., Ferreira, A. M., Kulessa, B., Schimmel, M., Berbellini, A., & Morelli, A. (2021). Uppermost crustal structure regulates the flow of the greenland ice sheet. *Nature communications*, *12*(1), 1–12.

Jordan, B. T., Grunder, A. L., Duncan, R. A., & Deino, A. L. (2004). Geochronology of age-progressive volcanism of the oregon high lava plains: Implications for the plume interpretation of yellowstone. *Journal of Geophysical Research: Solid Earth*, *109*(B10).

Laske, G., Masters, G., Ma, Z., & Pasyanos, M. (2012). Crust1. 0: An updated global model of earth's crust. *Geophys Res Abs*, *14*, 3743.

Laske, G., Masters, G., Ma, Z., & Pasyanos, M. (2013). Update on crust1. 0—a 1-degree global model of earth's crust. In *Geophys. res. abstr* (Vol. 15, p. 2658).

Lin, F.-C., Moschetti, M. P., & Ritzwoller, M. H. (2008). Surface wave tomography of the western united states from ambient seismic noise: Rayleigh and love wave phase velocity maps. *Geophysical Journal International*, *173*(1), 281–298.

Lin, F.-C., Tsai, V. C., & Ritzwoller, M. H. (2012). The local amplification of surface waves: A new observable to constrain elastic velocities, density, and anelastic attenuation. *Journal of Geophysical Research: Solid Earth*, *117*(B6).

Lin, F.-C., Tsai, V. C., & Schmandt, B. (2014). 3-d crustal structure of the western united states: application of rayleigh-wave ellipticity extracted from noise cross-correlations. *Geophysical Journal International*, *198*(2), 656–670.

Masters, G., Woodhouse, J., & Freeman, G. (2011). Mineos v1. 0.2 [software]. *Computational Infrastructure for Geodynamics*.

Moschetti, M., Ritzwoller, M., Lin, F., & Yang, Y. (2010b). Seismic evidence for widespread western-us deep-crustal deformation caused by extension. *Nature*, *464*(7290), 885–889.

Moschetti, M., Ritzwoller, M., Lin, F.-C., & Yang, Y. (2010a). Crustal shear wave velocity structure of the western united states inferred from ambient seismic noise and earthquake data. *Journal of Geophysical Research: Solid Earth*, *115*(B10).

Moschetti, M., Ritzwoller, M., & Shapiro, N. (2007). Surface wave tomography of the western united states from ambient seismic noise: Rayleigh wave group velocity maps. *Geochemistry, Geophysics, Geosystems*, *8*(8).

Pasyanos, M. E., Masters, T. G., Laske, G., & Ma, Z. (2014). Litho1. 0: An updated crust and lithospheric model of the earth. *Journal of Geophysical Research: Solid Earth*, *119*(3), 2153–2173.

Porter, R., Liu, Y., & Holt, W. E. (2016). Lithospheric records of orogeny within the continental us. *Geophysical Research Letters*, *43*(1), 144–153.

Rudnick, R., & Gao, S. (2014). Composition of the continental crust, in Treatise on Geochemistry. *Elsevier, San Diego, Calif.*, *4*, 1–51.

Sambridge, M. (1999). Geophysical inversion with a neighbourhood algorithm—i. searching a parameter space. *Geophysical journal international*, *138*(2), 479–494.

Schaeffer, A., & Lebedev, S. (2015). Global heterogeneity of the lithosphere and underlying mantle: A seismological appraisal based on multimode surface-wave dispersion analysis, shear-velocity tomography, and tectonic regionalization. In *The earth's heterogeneous mantle* (pp. 3–46). Springer.

Schardong, L., Ferreira, A. M., Berbellini, A., & Sturgeon, W. (2019). The anatomy of uppermost mantle shear-wave speed anomalies in the western us from surface-wave amplification. *Earth and Planetary Science Letters*, *528*, 115822.

Schardong, L., Sturgeon, W., Ferreira, A. M., & Berbellini, A. (2022, November). *WUSA surface wave amplification measurements (Schardong et al. 2019).* Zenodo. Retrieved from `https://doi.org/10.5281/zenodo.7352566` doi: 10.5281/zenodo.7352566

Schellart, W., Stegman, D., Farrington, R., Freeman, J., & Moresi, L. (2010). Cenozoic tectonics of western north america controlled by evolving width of farallon slab. *Science*, *329*(5989), 316–319.

Schmandt, B., & Humphreys, E. (2011). Seismically imaged relict slab from the 55 ma siletzia accretion to the northwest united states. *Geology*, *39*(2), 175–178.

Schmandt, B., Lin, F.-C., & Karlstrom, K. E. (2015). Distinct crustal isostasy trends east and west of the rocky mountain front. *Geophysical Research Letters*, *42*(23), 10–290.

Shapiro, N. M., Campillo, M., Stehly, L., & Ritzwoller, M. H. (2005). High-resolution surface-wave tomography from ambient seismic noise. *Science*, *307*(5715), 1615–1618.

Shen, W., & Ritzwoller, M. H. (2016). Crustal and uppermost mantle structure beneath the united states. *Journal of Geophysical Research: Solid Earth*, *121*(6), 4306–4342.

Shen, W., Ritzwoller, M. H., & Schulte-Pelkum, V. (2013). A 3-d model of the crust and uppermost mantle beneath the central and western us by joint inversion of receiver functions and surface wave dispersion. *Journal of Geophysical Research: Solid Earth*, *118*(1), 262–276.

Smith, R., Schilly, M., Braile, L., Ansorge, J., Lehman, J., Baker, M., ... Greensfelder, R. (1982). The 1978 yellowstone-eastern snake river plain seismic profiling experiment: Crustal structure of the yellowstone region and experiment design. *Journal of Geophysical Research: Solid Earth*, *87*(B4), 2583–2596.

Sparlin, M. A., Braile, L., & Smith, R. B. (1982). Crustal structure of the eastern snake river plain determined from ray trace modeling of seismic refraction data. *Journal of Geophysical Research: Solid Earth*, *87*(B4), 2619–2633.

Stewart, J. H. (1980). Geology of nevada. *Nevada Bureau of Mines and Geology special publication*, *4*, 136.

Szwillus, W., Afonso, J. C., Ebbing, J., & Mooney, W. D. (2019). Global crustal thickness and velocity structure from geostatistical analysis of seismic data. *Journal of Geophysical Research: Solid Earth*, *124*(2), 1626–1652.

Taylor, S. R., Gerstoft, P., & Fehler, M. C. (2009). Estimating site amplification factors from ambient noise. *Geophysical research letters*, *36*(9).

Tesauro, M., Kaban, M. K., Mooney, W. D., & Cloetingh, S. (2014). Nacr14: A 3d model for the crustal structure of the north american continent. *Tectonophysics*, *631*, 65–86.

van Heijst, H. J., & Woodhouse, J. (1997). Measuring surface-wave overtone phase velocities using a mode-branch stripping technique. *Geophysical Journal International*, *131*(2), 209–230.

Voronoï, G. (1908). Nouvelles applications des parametres continus a la theorie des forms quadratiques. deuxieme memoire: Recheches sur les parallelloedres primitifs. *J. reine angew. Math.*, *134*, 198–287.

Walker, J. D., Bowers, T. D., Glazner, A. F., Farmer, A., & Carlson, R. W. (2004). Creation of a north american volcanic and plutonic rock database (navdat). In *Geological society of america abstracts with programs* (Vol. 36, p. 9).

Wessel, P., & Smith, W. H. (1998). New, improved version of generic mapping tools released. *Eos, Transactions American Geophysical Union*, *79*(47), 579–579.

Xie, J., Chu, R., & Yang, Y. (2018). 3-d upper-mantle shear velocity model beneath the contiguous united states based on broadband surface wave from ambient seismic noise. *Pure and Applied Geophysics*, *175*(10), 3403–3418.

Yudistira, T., Paulssen, H., & Trampert, J. (2017). The crustal structure beneath the netherlands derived from ambient seismic noise. *Tectonophysics*, *721*, 361–371.

Zandt, G., Myers, S. C., & Wallace, T. C. (1995). Crust and mantle structure across the basin and range-colorado plateau boundary at 37 n latitude and implications for cenozoic extensional mechanism. *Journal of Geophysical Research: Solid Earth*, *100*(B6), 10529–10548.

Supporting Information for "Crustal structure of the Western U.S. from Rayleigh and Love wave amplification"

William Sturgeon[1], Ana M.G. Ferreira[1,2], Lewis Schardong[3], Augustin Marignier[1,4]

[1]Department of Earth Sciences, Faculty of Mathematical & Physical Sciences, University College London, WC1E 6BT, UK

[2]CERIS, Instituto Superior Técnico, Universidade de Lisboa, Av. Rovisco Pais 1, 1049-001 Lisboa, Portugal

[3]The Geological Survey of Israel, Jerusalem, Israel

[4]Mullard Space Science Laboratory, University College London, RH5 6NT, UK

Contents of this file

1. Figures S1 to S12
2. Table S1

References

Chai, C., Ammon, C. J., Maceira, M., & Herrmann, R. B. (2015). Inverting interpolated receiver functions with surface wave dispersion and gravity: Application to the western us and adjacent canada and mexico. *Geophysical Research Letters*, *42*(11), 4359–4366.

Crotwell, H. P., & Owens, T. J. (2005). Automated receiver function processing. *Seismological Research Letters*, *76*(6), 702–709.

Laske, G., Masters, G., Ma, Z., & Pasyanos, M. (2012). Crust1. 0: An updated global model of earth's crust. *Geophys Res Abs*, *14*, 3743.

Moschetti, M., Ritzwoller, M., Lin, F.-C., & Yang, Y. (2010). Crustal shear wave velocity structure of the western united states inferred from ambient seismic noise and earthquake data. *Journal of Geophysical Research: Solid Earth*, *115*(B10).

Porter, R., Liu, Y., & Holt, W. E. (2016). Lithospheric records of orogeny within the continental us. *Geophysical Research Letters*, *43*(1), 144–153.

Sambridge, M. (1999). Geophysical inversion with a neighbourhood algorithm—i. searching a parameter space. *Geophysical journal international*, *138*(2), 479–494.

Schardong, L., Ferreira, A. M., Berbellini, A., & Sturgeon, W. (2019). The anatomy of uppermost mantle shear-wave speed anomalies in the western us from surface-wave amplification. *Earth and Planetary Science Letters*, *528*, 115822.

Schmandt, B., Lin, F.-C., & Karlstrom, K. E. (2015). Distinct crustal isostasy trends east and west of the rocky mountain front. *Geophysical Research Letters*, *42*(23), 10–290.

Shen, W., & Ritzwoller, M. H. (2016). Crustal and uppermost mantle structure beneath the united states. *Journal of Geophysical Research: Solid Earth*, *121*(6), 4306–4342.

Xie, J., Chu, R., & Yang, Y. (2018). 3-d upper-mantle shear velocity model beneath the contiguous united states based on broadband surface wave from ambient seismic noise. *Pure and Applied Geophysics*, *175*(10), 3403–3418.

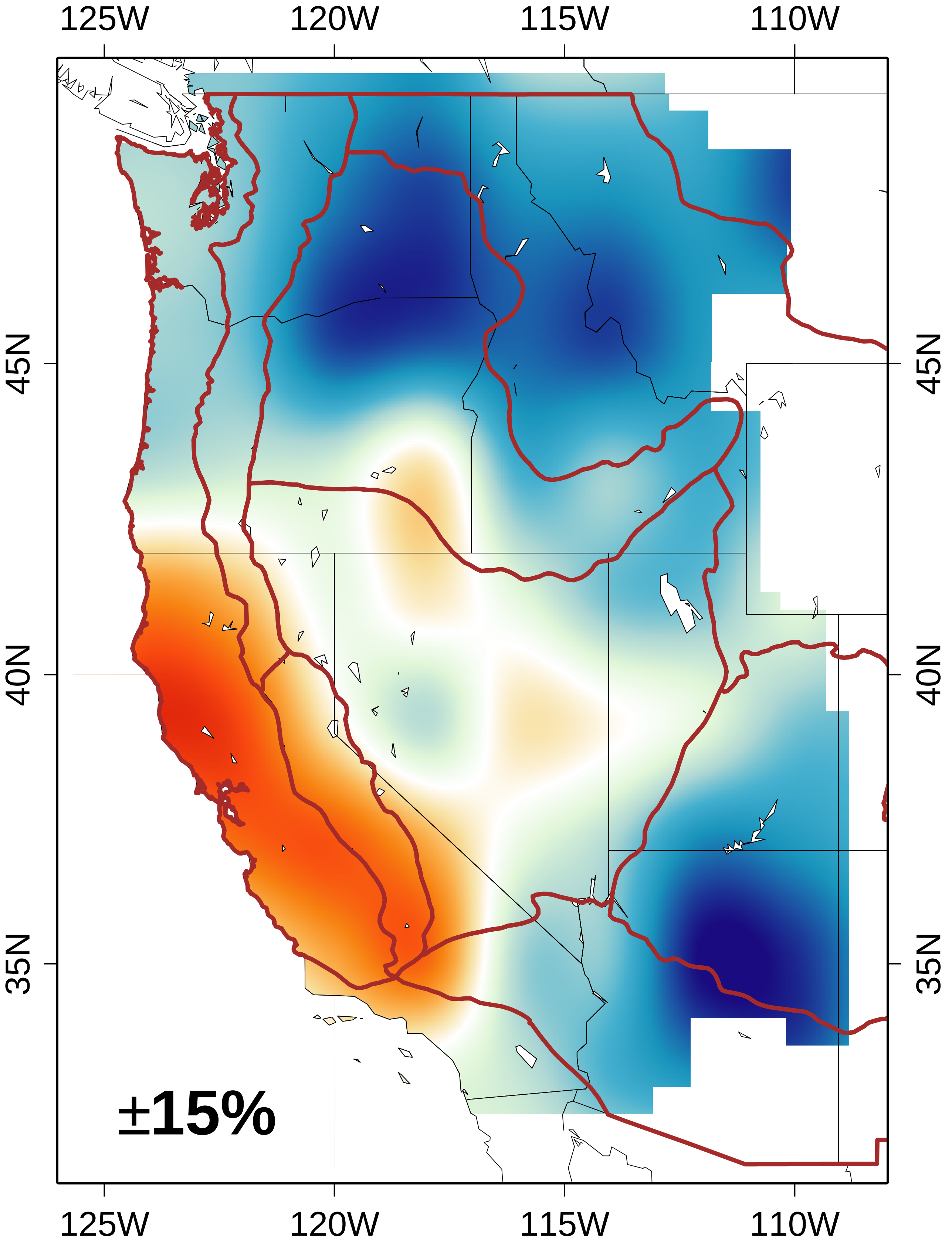

Figure S1. The crustal layer of SWUS-amp Schardong et al. (2019), shown in percentage perturbations from the averaged crustal v_S, where the maximum and minimum perturbations are 15%.

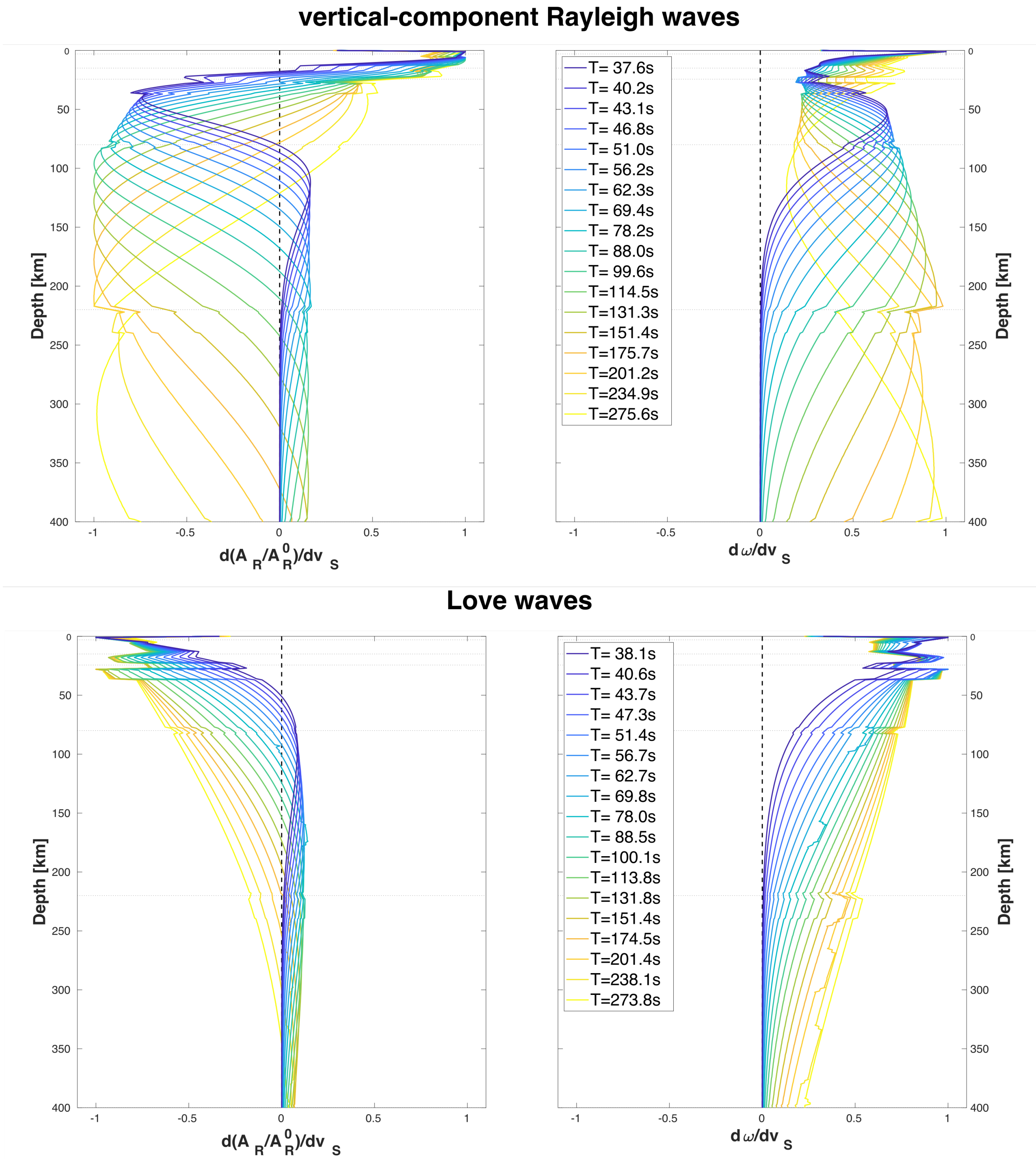

Figure S2. Sensitivity kernels of amplification (left) and phase velocity (right) to v_S for vertical-component Rayleigh waves (top row) and Love waves (bottom row) at all available periods.

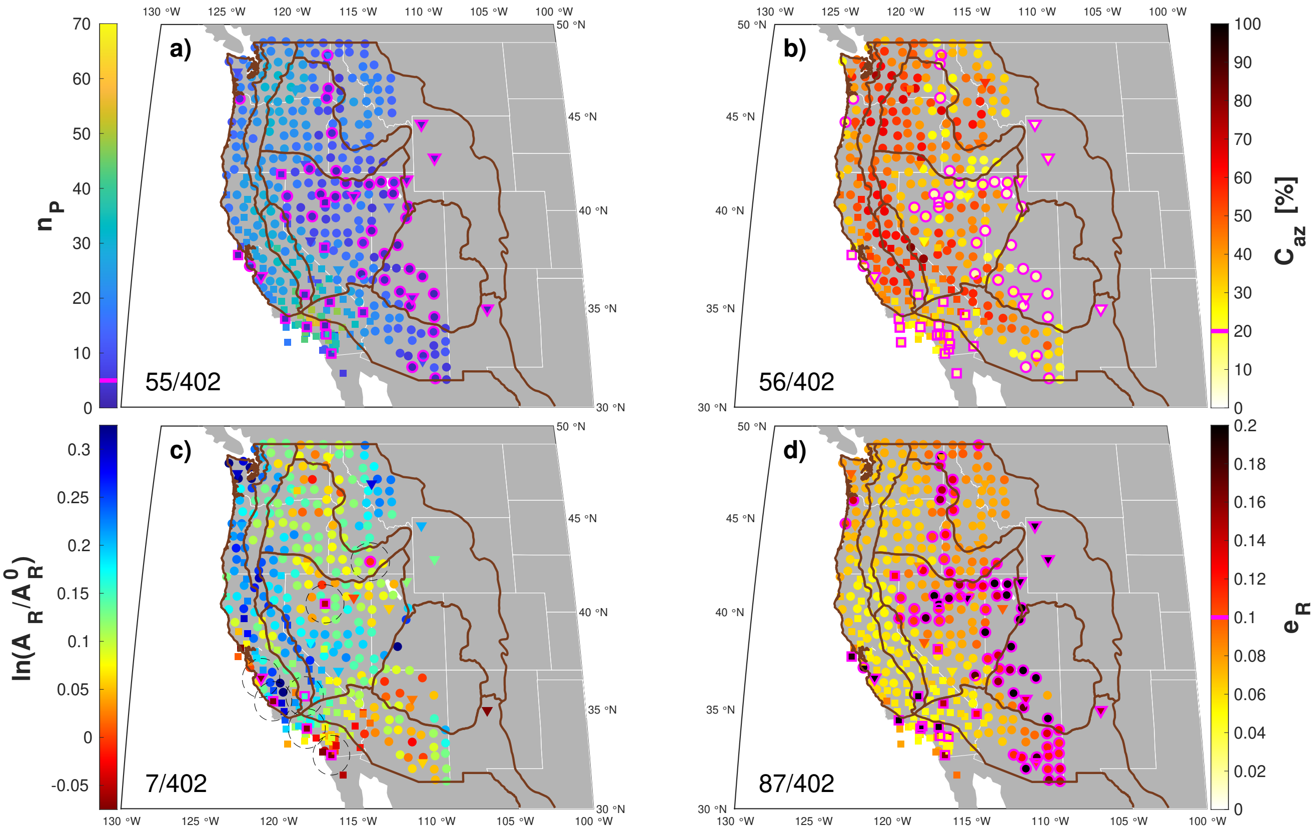

Figure S3. The selection process for fundamental mode Love wave local amplification at 38 s. From top-left to bottom-right, each sub-figure represents (a) selection upon the number of station pairs used to invert for local amplification at each receiver, (b) selection upon the azimuthal coverage of the station pairs used to invert for local amplification at each receiver, (c) elimination of outliers based on local geographical coherency, and (d) selection upon the error on amplification factors. Symbols outlined in magenta on the maps represent discarded stations (the number of discarded stations is shown in the numerator in the bottom-left corner of each sub-figure and the number in the denominator is the total number of stations), and magenta ticks on the colour bars represent the selection threshold when applicable.

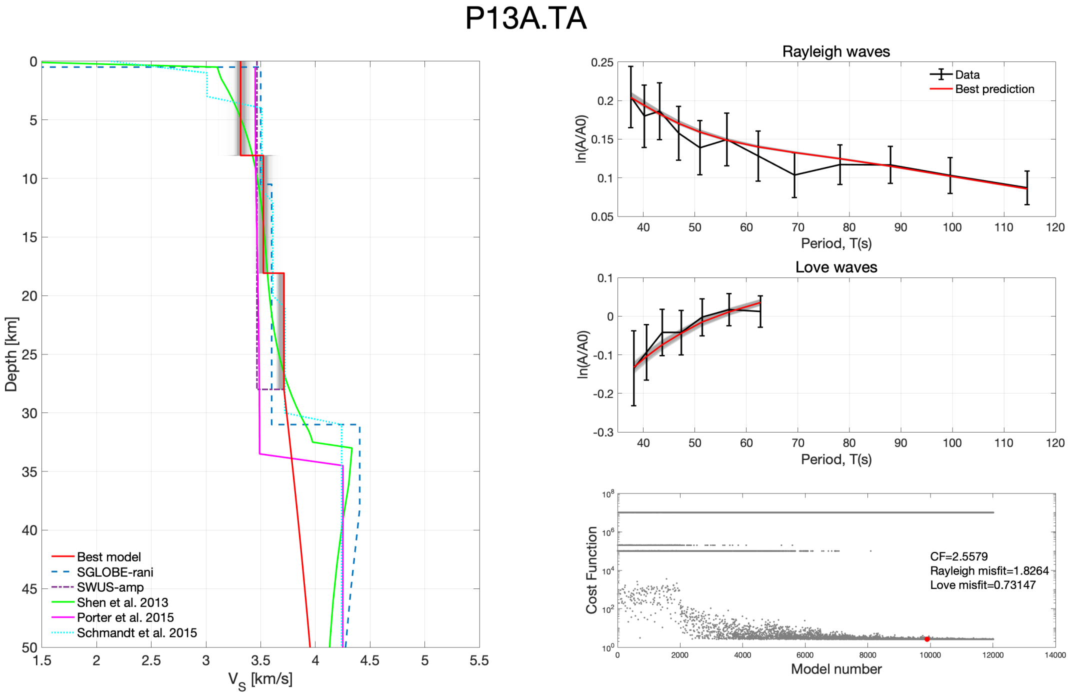

Figure S4. Example of an inversion using the Neighbourhood Algorithm (Sambridge, 1999) for stations P13A.TA. Left: 1D profile of V_S against depth for this study (red line) and other studies (coloured lines, as shown in legend). Top right: Rayleigh wave amplification curves. Middle right: Love wave amplification curves. Bottom right: cost-function evolution for the inversion, the red dot corresponds to the model with the lowest misfit.

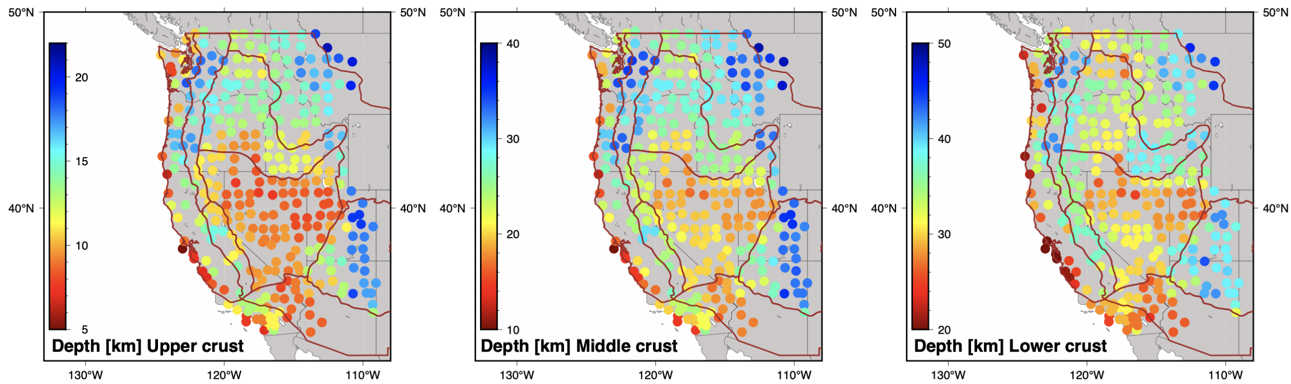

Figure S5. The depths of each crustal layer beneath each station used in this study. Depths are defined by those in CRUST1.0 (Laske et al., 2012)

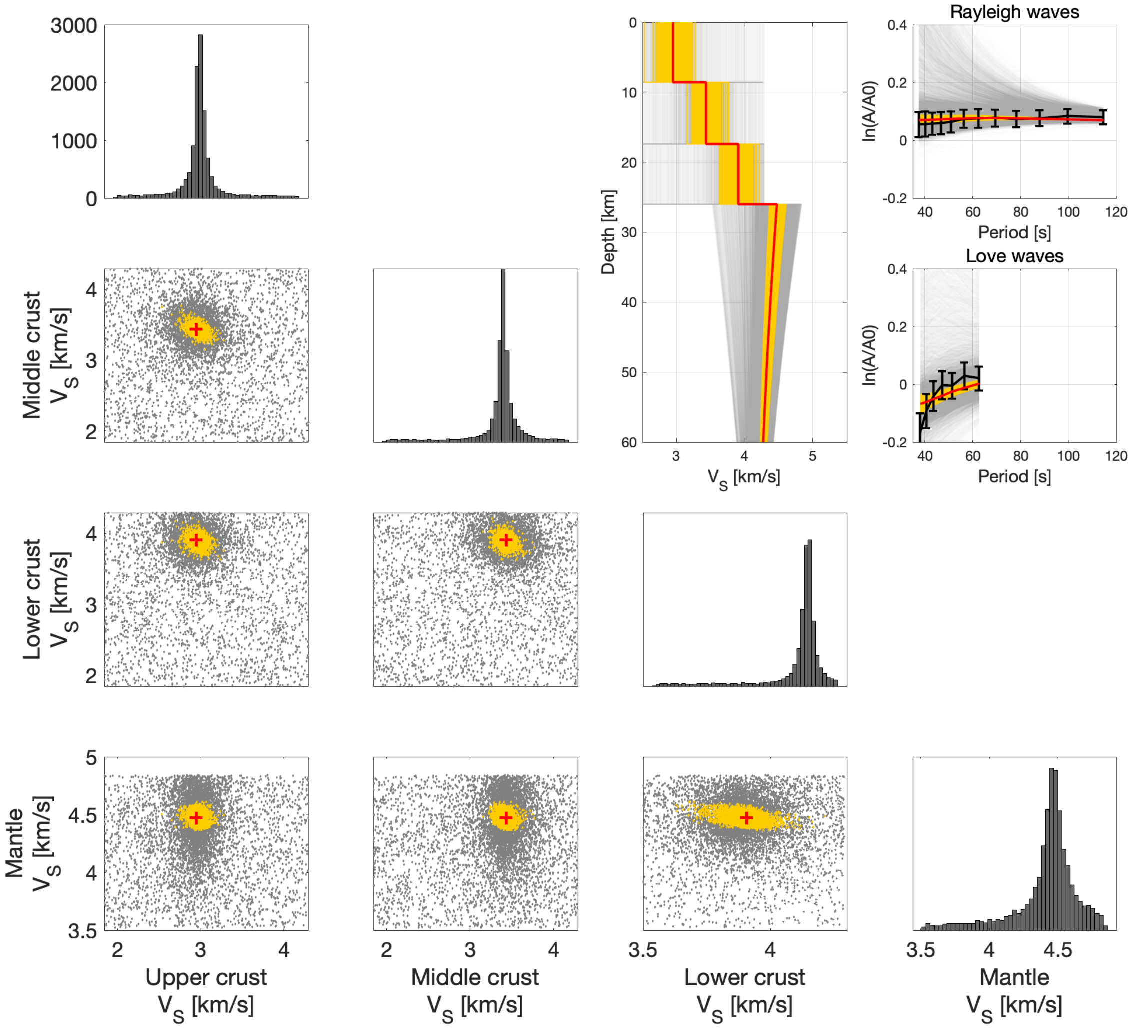

Figure S6. Example of parameter trade-offs for the station TA.Y13A. We show the trade-off in V_S for the upper crust, middle crust, lower crust, and uppermost mantle. The uppermost mantle is defined as being between the moho depth (35km) to ∼100 km. We perturb the uppermost mantle V_S using a single spline in this depth range. Histograms are also included for each parameter. Red lines and crosses represent the model with the lowest misfit, yellow lines and dots represent models with 20% of the best model and grey lines and dots represent all models search in the inversion.

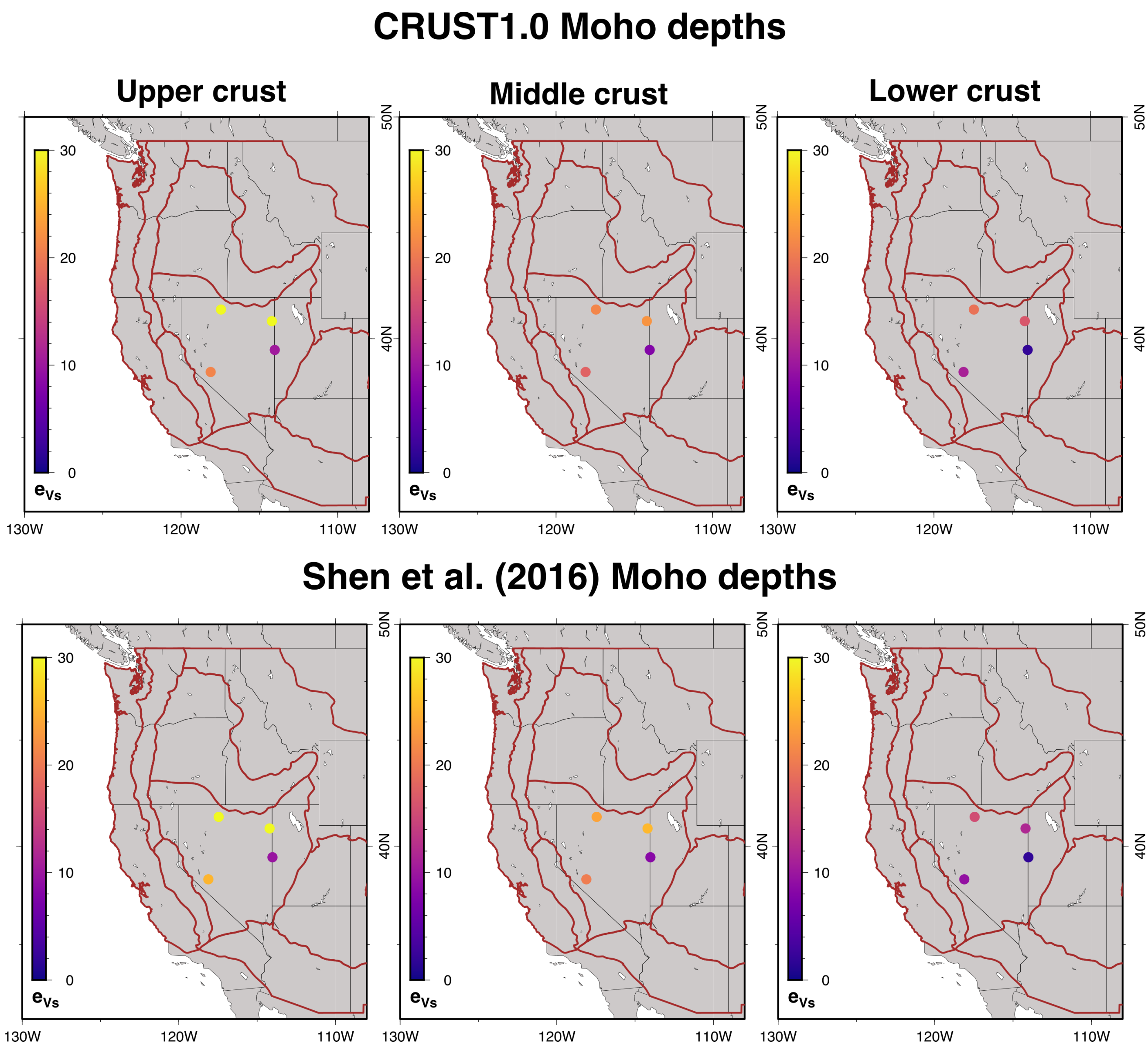

Figure S7. Uncertainty of station shear-wave velocity for four stations in the North Basin and Range, as given by Equation 8 in the main manuscript. Top row: Uncertainty of station velocity when defining the depth of each crustal layer using the model CRUST1.0 (Laske et al., 2012). Bottom row: the same as the top row but using the crustal depths from (Shen & Ritzwoller, 2016).

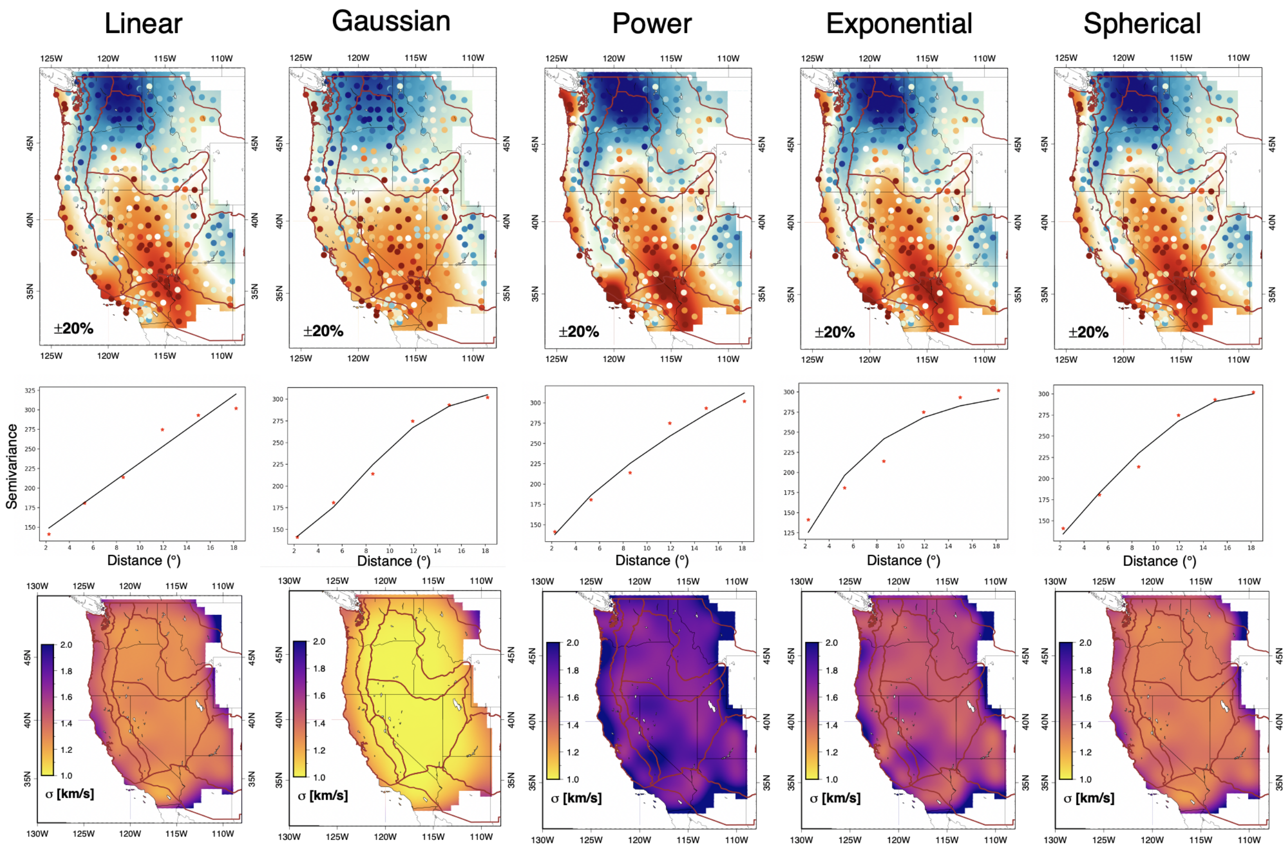

Figure S8. Ordinary kriging analysis in the upper crustal layer. We explore the effects of using a linear, gaussian, power, exponential and spherical model parameterisation to fit the semi-variogram. Top row: stations coloured by perturbations in v_S from the average v_S in the layer, and the interpolated map behind. Note the limits of the perturbations are given in the bottom left corner. Middle row: the respective semi-variograms. Bottom row: standard deviation of the kriging interpolation of perturbations of v_S from the average value in the layer.

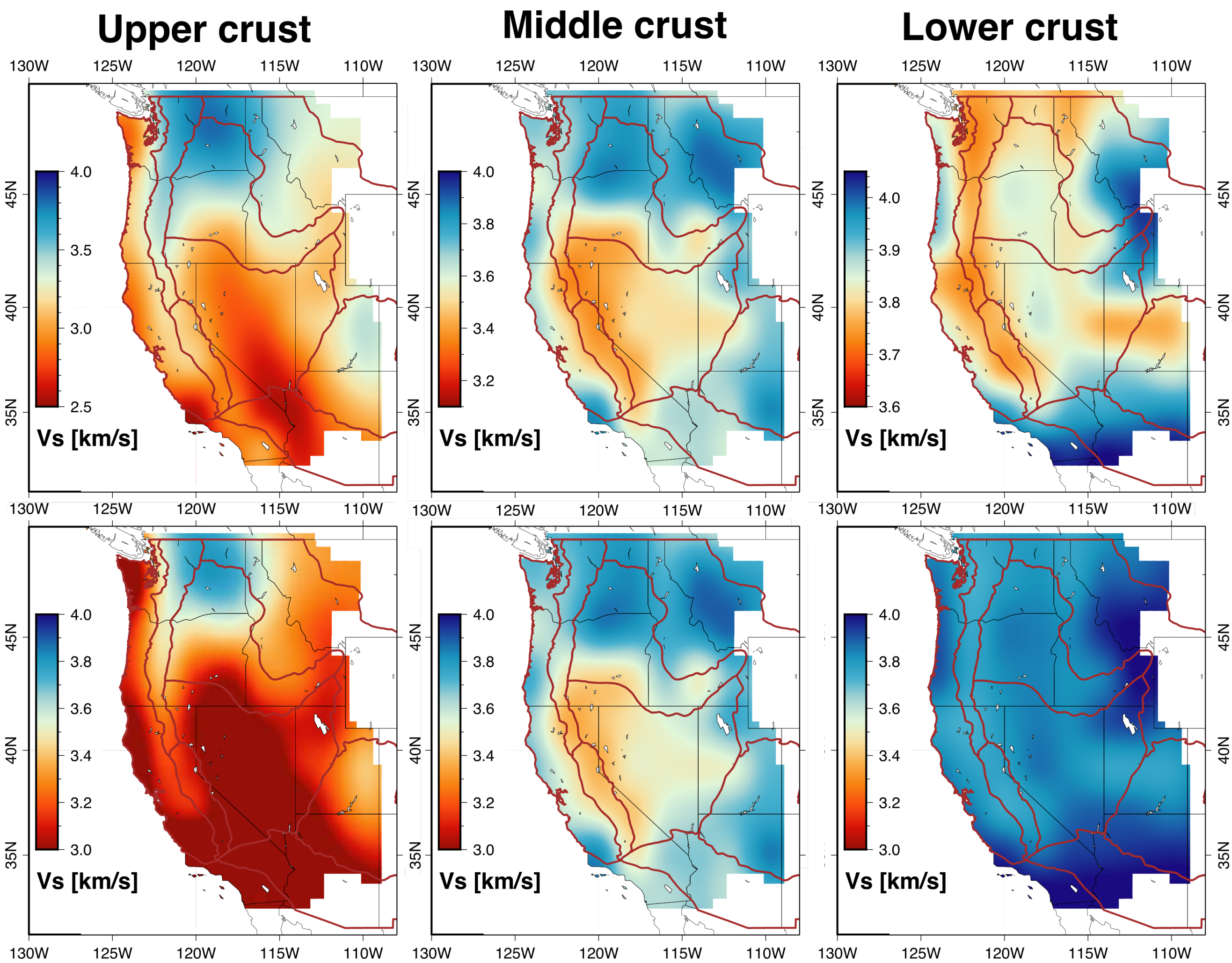

Figure S9. Top row: SWUS-crust absolute v_S plotted with different colour scales to further highlight the various features in the model. Bottom row: the same as the top row but with the scale fixed across all layers.

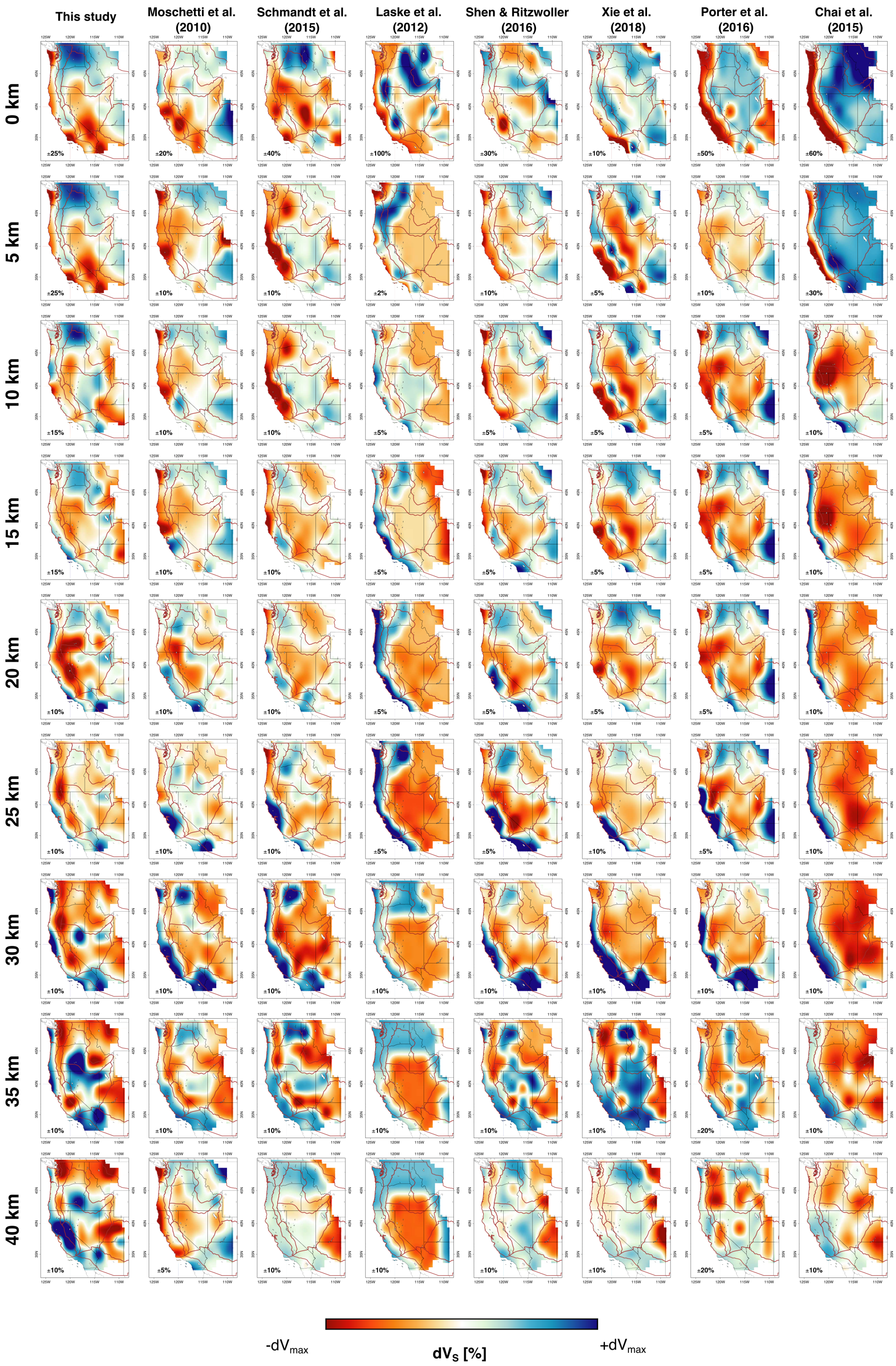

Figure S10. Comparison of the SWUS-crust v_S model (first column) with other local tomographic models Moschetti et al. (2010); Schmandt et al. (2015); Laske et al. (2012); Shen and Ritzwoller (2016); Xie et al. (2018); Porter et al. (2016); Chai et al. (2015) at crustal depths. The velocity perturbations of all models are expressed with respect to the average velocity at each depth respectively. The limits of the colour scale of each model and at each depth are displayed in the bottom left corner of each map. Boundaries of tectonic provinces are represented by solid light brown lines. The lateral extents of our model is also added to each model in order to aid in their comparisons.

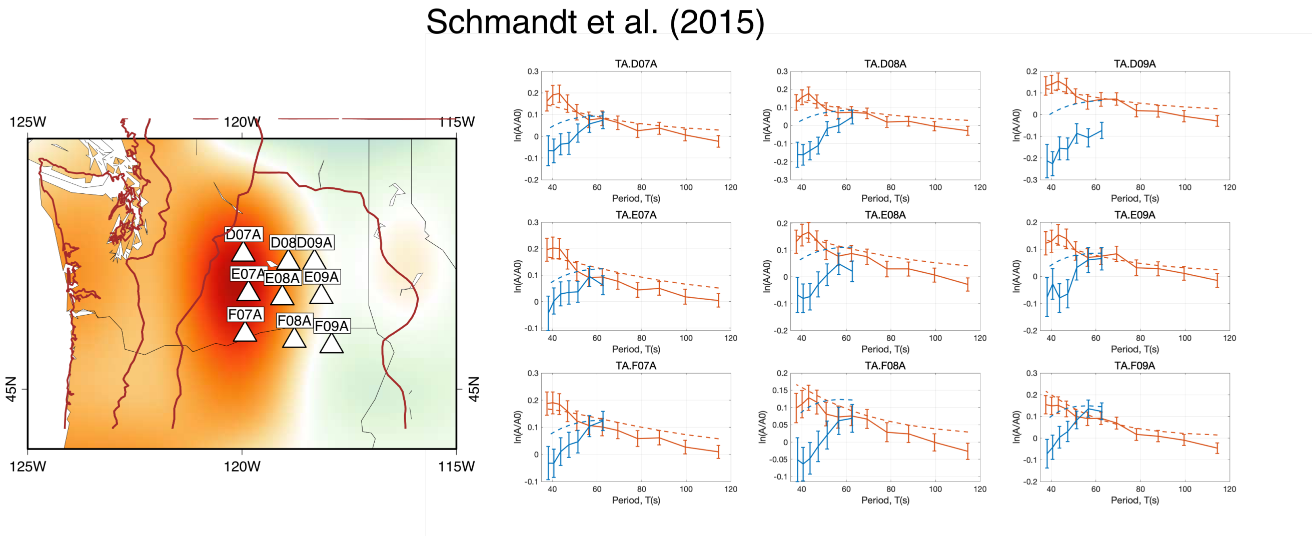

Figure S11. Prediction of amplification curves when using shear wave velocities from Shen and Ritzwoller (2016). Left: Map of Schmandt et al. (2015) in the upper crustal layer centred centred on the Columbia Basin and the location of the 9 stations used in this test. Right: Amplification curves for vertical-component Rayleigh waves (red curves) and Love waves (blue curves). The observed data are shown as solid lines with error bars, and the theoretical curves are shown as dashed lines.

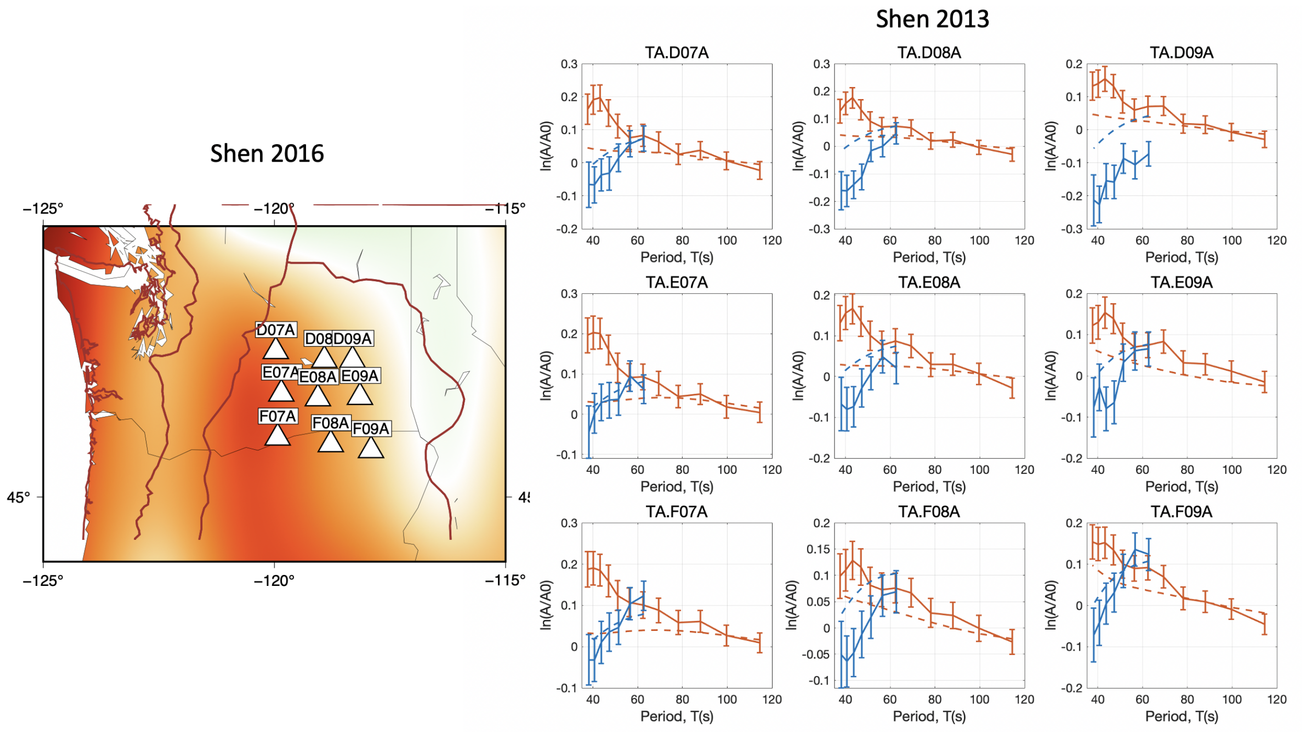

Figure S12. Prediction of amplification curves when using shear wave velocities from Shen and Ritzwoller (2016). Left: Map of Shen and Ritzwoller (2016) at 5 km depth centred on the Columbia Basin and the location of the 9 stations used in this test. Right: Amplification curves for vertical-component Rayleigh waves (red curves) and Love waves (blue curves). The observed data are shown as solid lines with error bars, and the theoretical curves are shown as dashed lines.

Table S1. Descriptions of the tomographic models analysed in this study.

Model	Datasets	Parameterisation		Forward modelling	3D inverse modelling & constraints
		Vertical	Horizontal		
CRUST1.0 (Laske et al., 2012)	Crustal thickness from active source seismic studies, receiver functions and gravity constraints v_s scaled from crustal types	Three crustal crystalline layers	1x1 degree cells	Compilation of existing datasets	
Moschetti et al. (2010)	Surface wave dispersion measurements from ambient seismic noise and teleseismic earthquakes (T 6-100s)	Three crustal layers	Interpolation of 1D profiles on 0.5° grid	Normal mode formalism	Monte Carlo inversion scheme Apriori v_P, v_S sediment and crustal thickness constraints
Schmandt et al. (2015)	Receiver functions Rayleigh wave phase velocity measurements (T 8-100 s) Rayleigh wave ellipticity maps (T 8-100s)	Three layered crust	Interpolated 1D profiles	Normal mode formalism?	Steepest descent No explicit regularisation
Shen and Ritzwoller (2016)	Rayleigh wave phase velocity measurements (T8-40 s, T28-80 s) Rayleigh wave group velocities (T8-28 s) Rayleigh wave ellipticity measurements (T 18-80s) Receiver functions	Four cubic B-splines	Kriging interpolation	Normal mode formalism?	.. Joint Bayesian Monte Carlo inversion Positive velocity jumps/gradients with depth Scaled v_P and density
Porter et al. (2016)	Rayleigh wave phase velocities (T 8-40 s) Wave gradiometry (T 20-150 s)	Crustal thickness estimates from the EarthScope Automated Receiver function Survey (EARS) Crotwell and Owens (2005)	0.25° grid	Normal mode formalism	Iterative linearised least squares inversion Damping applied
Xie et al. (2018)	Phase velocity measurements (T 10-150 s)	Four B-splines	Interpolation on 5° grid	Normal mode formalism	Non-linear MCMC inversion Increasing v_S with crustal depth
Chai et al. (2015)	Rayleigh wave group velocities (T 7-250 s) Bouger gravity observations P wave receiver functions	Smooth 1D profiles	1° cells	Finite difference approximations	Iterative linearised discrete inversion with smoothness-based stabilisation v_S increases with depth